Geochemical investigation of serpentinized oceanic lithospheric mantle in the Feather River Ophiolite, California: Implications for the recycling rate of water by subduction

Zheng-Xue Anser Li *, Cin-Ty Aeolus Lee

Department of Earth Sciences, MS-126, Rice University, 6100 Main St., Houston, TX, 77005, USA

Abstract

The petrology and geochemistry of serpentinized harzburgites within the Feather River Ophiolite in northern California were investigated to constrain the origin of serpentinization. Trace-element systematics indicate that serpentinization was associated almost solely with relatively low temperature hydrothermal addition of seawater and not with the addition of metamorphic fluids associated with subduction or tectonic obduction. Major element systematics show almost negligible disturbance, suggesting low water/rock ratios rather than the very high water/rock ratios characteristic of serpentinization of exhumed mantle at the seafloor such as seen in abyssal peridotites. These observations were taken to indicate that serpentinization occurred by the addition of seawater to ultramafic protoliths while they were structurally within the oceanic lithosphere prior to tectonic accretion.

Major and trace element systematics were used with simple melting models and assumptions about the thermal state of the mantle to put rough constraints on the paleo-depths at which the ultramafic protoliths were the last melted. Assuming that these peridotites were formed beneath a passive upwelling system, these paleo-melting depths were assumed to equate with paleo-serpentinization depths. For a model mantle potential temperature of 1350 °C, the paleo-serpentinization depth was estimated to be at least ~40 km based on the minimum melting degree observed in the Feather River Ophiolite peridotites. This depth constraint on serpentinization was then combined with model estimates of the lateral extent of serpentinization assuming that serpentinization is associated with infiltration of water through faults and fractures. If these observations can be generalized, we estimate that recycling rate of serpentine-bound water in subduction zones is roughly one order of magnitude higher than that associated with mineralogically bound water in subducting oceanic crust and sediments. After accounting for serpentine recycling, it is shown that the recycling rate of water via subduction is roughly equal to the global volcanic dewatering rate, suggesting that the water budget of the ocean and Earth's interior may presently be close to steady state.
© 2006 Elsevier B.V. All rights reserved.

Keywords: Feather River Ophiolite; Lithospheric mantle; Serpentinization; Subduction; Water recycling rate

1. Introduction

Serpentinization of oceanic lithosphere is of interest to geoscientists because it influences the recycling of water and certain fluid-mobile elements (such as F, Cl,

* Corresponding author. Tel.: +1 713 348 3272.
  E-mail address: zxli@rice.edu (Z.-X.A. Li).

and B) during subduction (Leeman, 1996; Straub and Layne, 2003; Rüpke et al., 2004; Sharp and Barnes, 2004), the volume and composition of arc magmas, the occurrence of intra-slab earthquakes at subduction zones (Peacock, 1990; Kirby et al., 1996; Peacock and Wang, 1999), and possibly even the rheology of the upper mantle (Hirth and Kohlstedt, 1996, 2004). Although the water content of oceanic crust and sediments is relatively well-known (Peacock, 1990), the extent to which the oceanic lithospheric mantle is hydrated is poorly constrained. As the oceanic lithospheric mantle can range up to ten times the thickness of oceanic crust, this uncertainty translates to a large uncertainty in the recycling rate of mineralogically bound water at subduction zones. However, because of the general inaccessibility of oceanic lithospheric mantle, most of our constraints on mantle serpentinization come from remote-sensing tools. For example, seismic reflection studies of the bending zones of subducting slabs suggest that serpentinized fractures may extend to at least 20 km into the lithospheric mantle (Ranero et al., 2003). As another example, double seismic zones within subducting slabs have been linked to the dehydration of serpentine as the loci of seismicity appear to roughly follow the 600–700 °C isotherms where serpentine breaks down (Raleigh, 1967; Green and Houston, 1995; Kirby, 1995; Hacker et al., 2003). If this interpretation is correct, such data indirectly suggest that hydration of the oceanic lithospheric mantle may reach 50 km into the slab (Hacker et al., 2003). This interpretation, however, is complicated by the possibility that antigorite breakdown is not the only process that occurs around 600–700 °C. For example, this temperature interval might also correspond to a rheologic transition, such as a change from plastic to viscous behavior (Kohlstedt et al., 1995).

An independent, observation-based means of quantifying the vertical and lateral extent of serpentinization is thus essential. We conducted a systematic petrologic and geochemical study of serpentinized peridotite samples from the Feather River Ophiolite (FRO) in northern California, just south of the north fork of the American river. We demonstrate that, at least in this part of the ophiolite belt, serpentinization was most likely imparted by interaction with seawater and that the ultramafic protolith was serpentinized during structural residence within intact oceanic lithospheric mantle prior to tectonic obduction. In other words, the observed serpentinization is neither a product of exhumation or of hydration of fore-arc mantle wedge during subduction or obduction. The results, together with an anhydrous mantle melting model assuming passive upwelling, allow us to reconstruct the paleo-depths of these peri-

dotites within the oceanic lithosphere. We then consider various mechanisms by which water can be introduced into the deep lithosphere. These hypothetical mechanisms are used to build simple models for quantifying the lateral extent to which serpentinization can occur. Combined with our observation-based depth constraints on serpentinization, we then attempt to quantify the global recycling rate of water into the mantle at subduction zones.

2. Study area and samples

The Feather River Ophiolite (FRO) represents a north–south trending ultramafic belt, no more than 10 km wide, set within the larger western Sierra Nevada Metamorphic Belt, which makes up the western foothills of the northern Sierra Nevada mountain range in California (Fig. 1). The FRO separates Mesozoic and Paleozoic North American continental shelf metasediments to the east from Mesozoic oceanic and island arc rocks to the west (Moores, 1970; Ehrenberg, 1975; Weisenberg, 1979; Day et al., 1985; Edelman et al., 1989; Hacker and Peacock, 1990; Mayfield and Day, 2000). It is generally agreed that the FRO is a major tectonic suture formed by the closing of an oceanic basin, and accordingly, the accretion of an island arc terrane to the North American continent. Ophiolite belts from the southwest Sierra Nevada Foothills have been similarly interpreted (Saleeby, 1978). The age of the suture is not well-known, but most likely formed during Devonian times (Hacker and Peacock, 1990). From Triassic to late Cretaceous times, this region was intruded later by Sierran arc-related granitoid plutons associated with the subduction of the Farallon plate — late Mesozoic plutons occur both west and east of the suture in the northern part of the Western Sierra Nevada Metamorphic belt.

A number of authors have investigated various segments of the FRO (Ehrenberg, 1975; Hacker and Peacock, 1990; Mayfield and Day, 2000; Weisenberg, 1979). It has been interpreted to represent oceanic lithospheric mantle or sub-arc lithospheric mantle. The former interpretation is based on the observation that most of the lithologies necessary for an ophiolite section are present. The latter interpretation, however, is based on a suggestion that the Feather River ultramafics are similar to Trinity ultramafics in the Klamath Mountains to the north and that, in the Klamaths, there appears to be an inverted metamorphic gradient in the metamorphic belt west of the Trinity ultramafics (Hacker and Peacock, 1990). Hacker and Peacock (1990) have suggested that peak $P–T$ conditions in both the Klamaths and the FRO are 500 to 650 ± 50 °C and 500 ± 300 MPa.
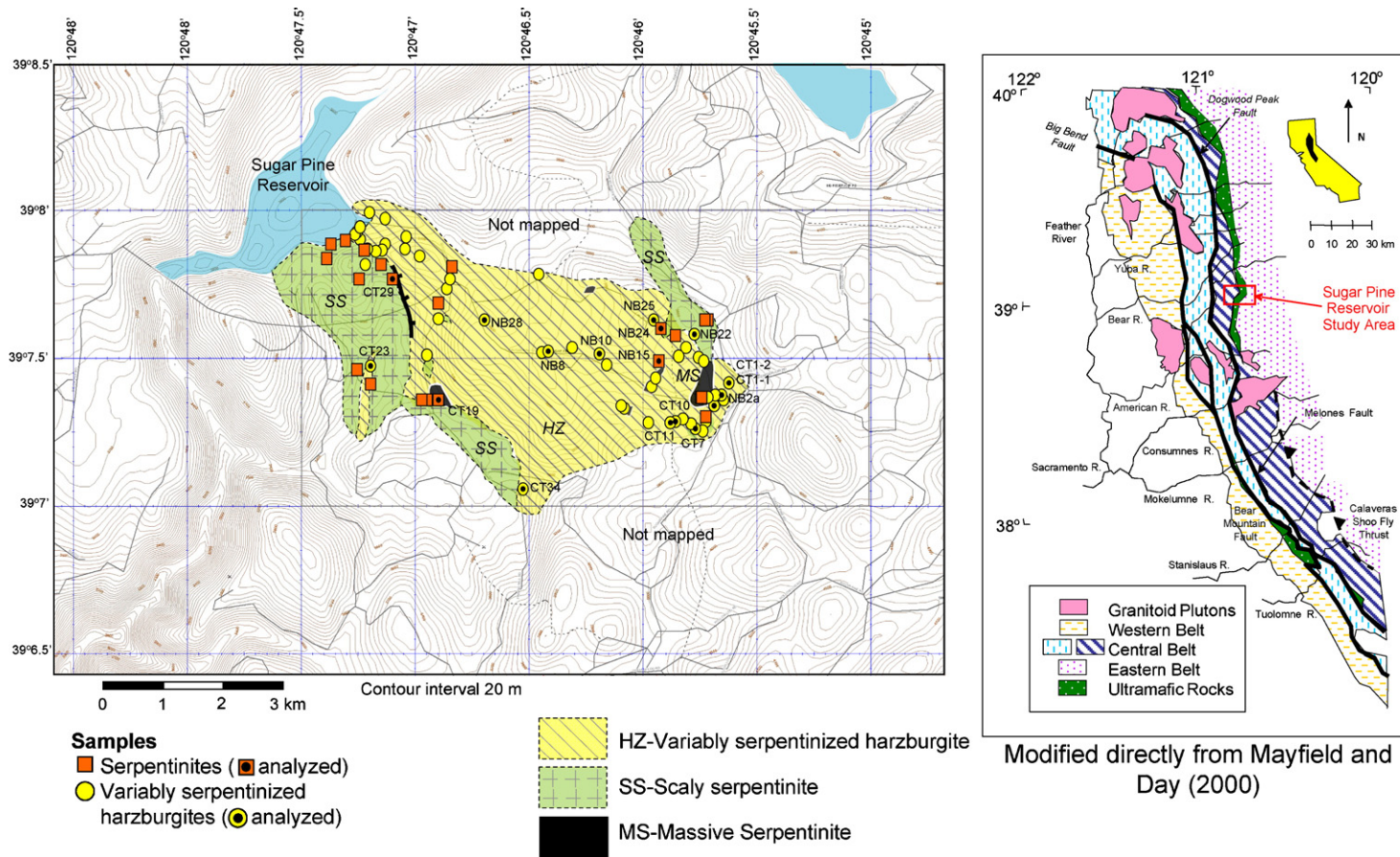
Fig. 1. Maps of the Sugar Pine Reservoir area of the Feather River Ophiolite. Right: geologic map of the Sierra Nevada Metamorphic Belt with the study area denoted by the squared region (modified from (Mayfield and Day, 2000)). Left: magnified map of Sugar Pine Reservoir study area. Sample locations denoted as circles and squares. Analyzed samples are denoted with black dots in the center of symbols. Sample names are also shown.

Table 1
XRF measurements, magnetite fraction, and calculated melt fraction

XRF	CT1-1	CT1-2	CT3	CT7	CT10	CT11	CT19	CT23	CT29
Unnormalized major elements (wt.%)									
SiO_2	42.71	42.82	42.16	42.03	42.18	42.59	42.54	42.7	43.26
Al_2O_3	0.99	1.18	0.86	1.54	0.64	0.71	1.98	2.29	0.73
TiO_2	0.01	0.017	0.011	0.019	0.005	0.004	0.023	0.013	0.006
FeO*	7.24	7.61	7.95	7.12	7.97	7.88	7.75	6.96	8.08
MnO	0.163	0.204	0.218	0.14	0.149	0.14	0.132	0.117	0.125
CaO	1.69	2.68	3.25	2.11	0.21	0.53	0.87	1.93	0.46
MgO	42.79	40.46	42.43	42.83	43.44	42.93	39.27	38.6	40.39
K_2O	0.01	0.02	0.02	0.02			0.01		0.01	
Na_2O	0.01	0.01	0.02	0.03			0.02	0.01	
P_2O_5	0.005	0.006	0.006	0.006	0.009	0.007	0.007	0.017	0.008
Total	95.62	95.01	96.92	95.84	94.6	94.82	92.58	92.64	93.06
Mg#	0.91	0.90	0.90	0.91	0.91	0.91	0.90	0.91	0.90
Unnormalized trace elements (ppm)									
Ni	2360	2209	2177	2238	2457	2508	2374	2253	2282
Cr	3438	2896	2566	3499	1731	2453	2709	2874	3127
Sc	11	11	11	8	7	7	9	13	9
V	43	51	47	42	29	29	42	62	32
Loss on ignition (LOI), magnetite fraction (M.F.) and estimated melt fraction (F)									
LOI (wt.%) (XRF)	7.95	9.37	5.12	7.18	9.79	9.52	13.5	13.2	12.7
M.F. (wt.%)	3.79	4.96	1.19	3.96	5.24	7.72	10.7	10	12.5
F (wt.%)	31.4	21.9	27.1	31.1	36.5	33.7	21.2	17.9	25.5

* denote the total Fe contents; Mg# is the molar Mg/(Mg+Fe*); *F* was estimated by interpolating the MgO of peridotites within pMELTs calculations.

Our study site is located in the Sugar Pine Reservoir area, just south of the north fork of the American River and is therefore situated further south than the above-mentioned studies conducted in the northern FRO (Fig. 1). The Sugar Pine Reservoir area was investigated in a reconnaissance study by Mayfield and Day (2000). Fig. 1 shows the location of our study site, along with a map of where our samples were collected. The study area consists only of ultramafic lithologies. As far as we can tell, the study area consists almost solely of harzburgitic lithologies having little to no clinopyroxene. Chromite-bearing dunites also occur, but are rare. We did not observe any dunite channels or pyroxenite veins as has been seen further north in the FRO and in the Trinity peridotite massif in the Klamath Range (Hacker and Peacock, 1990). The harzburgites have all been serpentinized to varying degrees. In some cases, serpentinization is complete, yielding massive serpentine with only minor relict peridotite structure. In other cases, the serpentinization was incomplete enough that original high-temperature peridotitic textures have been retained; in these samples, a few fresh olivine and pyroxene grains can actually be seen in hand-specimen. Unlike the Trinity ophiolite and some parts of the northernmost Feather River ophiolite (Ehrenberg, 1975;

Weisenberg, 1979; Hacker and Peacock, 1990), we found no field or petrographic evidence for talc, tremolite or anthophyllite. We also found no evidence for rodingite veins.

3. Analytical methods

Nineteen samples were selected randomly from a larger set of samples (Fig. 1) for geochemical analyses. Major and minor element concentrations (SiO_2, MgO, Al_2O_3, Cr_2O_3, MnO, FeO, Na_2O, and K_2O) as well as some trace elements were measured by X-ray fluorescence (XRF) spectroscopy at Washington State University, Pullman (Table 1). Loss on ignition (LOI), which is the fraction of mass lost by heating the sample to 900 °C, was determined for all samples *on separate powder aliquots* at WSU Pullman (Table 1). Because LOI was determined on separate aliquots, the sum of LOI and XRF total do not equal 100% and in many cases are greater than 100%. All data reported in Table 1 represent raw, unnormalized data. Magnetite (weight) concentrations estimated by magnetic separation were also determined (Table 1). Comprehensive trace element and selected major and minor element (Fe and Mn) concentrations were analyzed by single-collector,

CT34	NB2a	NB8	NB10	NB10b	NB15	NB22	NB24	NB25	NB28
42.57	42.54	42.06	43.1	42.57	41.56	42.51	43.33	43.74	44.44
1.95	0.9	1.71	0.92	1.85	0.9	0.99	1.13	1.19	1.49
0.024	0.008	0.023	0.007	0.035	0.002	0.015	0.017	0.02	0.014
6.44	7.4	8.69	6.9	7.43	11.3	7.82	7.85	7.11	4.12
0.154	0.149	0.157	0.107	0.108	0.127	0.197	0.105	0.135	0.347
1.57	0.47	1.54	0.03	1.21	0.19	3.23	0.41	0.99	0.02
40.13	43.22	39.85	41.76	39.3	38.33	41.73	39.95	39.55	41.67
0.01	0.01	0.02	0.01				0.01	0.01	0.03
		0.02	0.05			0.02			0.02
0.007	0.009	0.007	0.006	0.008	0.011	0.009	0.008	0.01	0.011
92.85	94.71	94.08	92.89	92.51	92.42	96.53	92.81	92.75	92.16
0.92	0.91	0.89	0.92	0.90	0.86	0.90	0.90	0.91	0.95
1947	2295	7437	2414	2958	3368	2311	2493	2342	3177
2912	3001	2927	3276	2957	3213	2975	2887	2986	3628
9	11	5	11	15	4	13	10	15	9
45	37	45	30	51	34	48	37	50	36
9.31	8.74	9.04	13	13.3	13.2	6	13.1	13.1	13
1.68	3.53	2.4	13.6	5.43	17.1	3.31	9.5	5.67	3.02
24.7	35.3	20.9	32.3	21.4	17.0	24.7	23.9	22.2	33.4

magnetic sector inductively coupled plasma mass spectrometry (ICP-MS) using a ThermoFinnigan Element II at Rice University (Table 2). Samples were crushed and powdered using a ceramic disk mill. Sample powders were dissolved as follows. A 0.08 g aliquot of sample powder was dissolved with a mixture of 0.5 mL concentrated Seastar HF and 1 mL concentrated Seastar $HClO_4$ in a 2.5 mL wrenchtop Teflon beaker at 115 °C for 12 h. The contents of the beaker were then dried down at 175 °C, and the dissolution repeated with 0.5 mL concentrated HF and 0.5 mL concentrated $HClO_4$. Samples were then subjected to a third and final acid attack using 0.5 mL $HClO_4$ only. The final dry down was taken up in 2 wt.% HNO_3 and diluted to 125 mL in a polyethylene bottle. A known amount of Indium tracer solution was added to the final dilution (to yield a concentration of 1 ppb) for use as an internal standard for instrumental drift. All samples were externally calibrated against the USGS BHVO-1 and BIR-1 international rock standards using reference values from Eggins et al. (1997). Peridotite standards JP-1 and DTS-2 were used for calibrating Ni contents. Reference standards were freshly prepared for each set of dissolutions following the same procedures for sample dissolution. A procedural blank was processed for every set of samples ana-

lyzed. Each sample was dissolved and analyzed twice. Most trace elements were analyzed in low mass resolution mode ($m / \Delta m = 300$). Some elements (Fe, Mn, Sc, V, Co) were measured in medium mass resolution mode ($m / \Delta m = 3000$) in order to resolve isobaric interferences.

4. Results

4.1. Petrography

All 19 samples are highly serpentinized (>90%) spinel harzburgites with only small amounts (<2%) of clinopyroxene present (Appendix Fig. 1). Serpentine pervasively occurs as a replacement product of olivines and pyroxenes, as anastomizing veins, and as cross-cutting veins. Serpentine and colorless chlorite also occurs as thin rims surrounding primary spinels; this feature was also seen by Ehrenberg (1975) and Hacker and Peacock (1990). Serpentine appears to be accompanied by the formation of fine-grained magnetite, which is concentrated in veins or along relict exsolution lamellae of pyroxenes. This is consistent with the rough correlation between LOI and magnetite content (Table 1). The former is a measure of water content in serpentine and the latter is a measure of how much secondary magnetite has been formed by

Table 2
ICP-MS measurements

ICP-MS	CT1-1		CT1-2		CT3		CT7		CT10		CT11		CT19		CT23		CT29		CT34	
ppm	run1	run2	run1	run2	run1	run2	run1	run2	run1	run2	run1	run2	run1	run2	run1	run2	run1	run2	run1	run2
Li	1.22	1.42	0.999	1.27	1.71	1.93	2.80	3.09	0.799	0.853	0.744	0.828	0.246	0.401	0.337	0.412	0.469	0.449	1.44	1.46
Be													0.0252		0.0244				0.0569	
Al(M)																				
P(M)	2.81	4.10	5.37	6.38	4.64	3.57	6.56	7.70	15.2	13.5	9.71	9.98	4.61	6.37		50.5	10.6		9.41	10.1
K(M)							97.6												87.6	
Ca(M)							14780												11790	
Sc(M)	10.4	11.2	13.1	14.1	12.3	13.3	11.2	11.5	7.78	6.78	8.84	9.01	10.0	10.7		14.1	6.09		11.4	12.1
Ti(M)	90.0	96.4	140	144	106	108	151	151	72.1	60.4	62.1	62.1	161	162		108	61.2		177	182
V(M)	45.4	46.6	58.9	59.1	53.8	54.8	51.6	53.3	28.6	24.2	32.9	32.0	48.9	50.4		57.9	26.2		47.8	50.0
Mn(M)	1289	1324	1632	1664	1708	1726	1052	1099	1281	1127	1088	1072	966	977		858	952		1137	1197
Fe(M)	60550	63780	64720	64790	65520	65640	59100	59280	72450	62890	65220	64620	56000	56600		54670	63650		50040	51380
Co(M)	121	126	127	127	126	121	117	118	146	128	129	129	113	116		106	118		134	138
Ni(M)	2373	2405	2342	2278	2229	2314	2311	2397	2768	2525	2428	2565	2120	2290		2215	2295		1810	2006
Cu(M)	3.37	4.88	11.1	10.2	4.66	5.65	3.72	2.56	2.80				12.5	10.5		8.61	8.69		9.55	9.05
Zn(M)	74.9	58.9	70.4	51.0	56.1	33.7	57.0	36.8	66.9	27.8	56.3	30.8	42.7	29.5		32.4	32.7		47.7	40.3
Ga	0.815	0.818	0.875	0.893	0.587	0.589	1.26	1.28	0.560	0.572	0.656	0.651	1.44	1.49	1.32	1.49	0.900	0.696	1.37	1.37
Rb	0.317	0.320	0.603	0.633	0.448	0.444	0.620	0.656	0.168	0.161	0.278	0.280	0.0756	0.0831	0.198	0.249	0.0374	0.0382	0.206	0.201
Sr	1.19	1.37	1.09	1.30	0.899	1.00	2.47	2.52	0.364	0.391	0.381	0.476	0.875	0.931	1.36	1.52	1.09	0.882	1.03	0.947
Y	0.350	0.364	0.680	0.729	0.501	0.515	0.770	0.761	0.112	0.107	0.189	0.193	0.974	1.01	0.881	1.22	0.170	0.156	1.16	1.07
Zr	0.238	0.450	0.256	0.305	0.435	0.431	0.462	0.456	0.380	0.278	0.492	0.390	0.759	0.566	0.896	0.337	1.92	0.411	2.08	2.07
Nb	0.0149	0.0521	0.0181		0.0203		0.0322	0.0198	0.0145		0.0150		0.0279						0.0237	
Cs	0.0328	0.0310	0.0777	0.0773	0.0304	0.0289	0.0423	0.0452	0.0130	0.0118	0.0177	0.0170	0.0111	0.0111	0.0211	0.0281	0.0076	0.0066	0.0141	0.0131
Ba	2.85	3.06	3.32	3.63	1.51	1.55	7.22	7.35	4.82	3.93	7.26	7.49	1.69	2.13	4.67	6.43	1.27	1.30	22.2	21.6
La	0.0564	0.0561	0.0513	0.0538	0.0334	0.0326	0.0213	0.0273	0.0148	0.0099	0.0521	0.0479	0.0048	0.0077	0.0236	0.0379	0.0087	0.0088	0.861	0.843
Ce	0.0642	0.0651	0.0739	0.0765	0.0465	0.0421	0.0448	0.0501	0.0279	0.0167	0.125	0.121	0.0083	0.0243	0.0486	0.0739	0.0195	0.0196	1.77	1.61
Pr	0.0054	0.0049	0.0057	0.0059	0.0041	0.0036	0.0049	0.0056	0.0030	0.0022	0.0105	0.0102	0.0050	0.0055	0.0075	0.0107	0.0028	0.0027	0.216	0.204
Nd	0.0169	0.0151	0.0178	0.0185	0.0166	0.0157	0.0266	0.0289	0.0119	0.0082	0.0411	0.0399	0.0533	0.0520	0.0390	0.0592	0.0142	0.0148	0.843	0.816
Sm	0.0087	0.0078	0.0152	0.0154	0.0106	0.0115	0.0200	0.0216	0.0030	0.0027	0.0091	0.0095	0.0394	0.0395	0.0223	0.0287	0.0076	0.0056	0.178	0.175
Eu	0.0058	0.0061	0.0086	0.0089	0.0043	0.0043	0.0127	0.0124	0.0037	0.0030	0.0062	0.0062	0.0116	0.0121	0.0112	0.0148	0.0061	0.0045	0.0530	0.0512
Tb	0.0040	0.0043	0.0081	0.0092	0.0056	0.0061	0.0079	0.0107	0.0010	0.0011	0.0024	0.0026	0.0125	0.0152	0.0127	0.0155	0.0022	0.0018	0.0298	0.0308
Gd	0.0165	0.0188	0.0341	0.0402	0.0235	0.0260	0.0337	0.0469	0.0045	0.0047	0.0132	0.0136	0.0651	0.0743	0.0516	0.0670	0.0095	0.0089	0.190	0.186
Dy	0.0368	0.0391	0.0745	0.0834	0.0514	0.0564	0.0739	0.0904	0.0100	0.0105	0.0207	0.0215	0.109	0.122	0.105	0.138	0.0173	0.0166	0.189	0.190
Ho	0.0124	0.0125	0.0249	0.0252	0.0177	0.0177	0.0259	0.0267	0.0038	0.0035	0.0066	0.0067	0.0317	0.0351	0.0283	0.0420	0.0048	0.0053	0.0425	0.0422
Er	0.0440	0.0438	0.0868	0.0867	0.0631	0.0631	0.0872	0.0895	0.0157	0.0141	0.0255	0.0240	0.106	0.116	0.0956	0.147	0.0181	0.0200	0.131	0.130
Tm	0.0085	0.0081	0.0156	0.0150	0.0118	0.0117	0.0148	0.0149	0.0033	0.0030	0.0049	0.0046	0.0167	0.0183		0.0250	0.0037		0.0208	0.0208
Yb	0.0566	0.0600	0.105	0.112	0.0787	0.0850	0.0871	0.0990	0.0250	0.0245	0.0328	0.0361	0.108	0.120	0.138	0.166	0.0443	0.0285	0.128	0.137
Lu	0.0110	0.0110	0.0193	0.0199	0.0140	0.0146	0.0155	0.0171	0.0053	0.0051	0.0062	0.0065	0.0181	0.0213	0.0196	0.0271	0.0059	0.0053	0.0206	0.0218
Hf	0.0044	0.0076	0.0087	0.0083	0.0094	0.0086	0.0118	0.0125	0.0027	0.0026	0.0056	0.0046	0.0197	0.0221	0.0069	0.0099	0.0035	0.0039	0.0683	0.0638
Ta		0.0088					0.0008	0.0051					0.0006	0.0013		0.0008	0.0004		0.0024	
Tl	0.0024		0.0032	0.0032	0.0031		0.0060	0.0029	0.0022		0.0041	0.0045	0.0044		0.0079	0.0057	0.0050		0.0397	0.0380
Pb					0.0998	0.0262	0.705	0.856	0.558		1.01	1.39		0.138	2.20	5.20	0.0707	0.149		0.369
Th	0.0071	0.0050	0.0032		0.0032		0.0028	0.0059	0.0032		0.0072		0.0021		0.0062	0.0097	0.0018		0.179	0.172
U	0.0016	0.0021	0.0012	0.0015	0.0053	0.0057	0.0032	0.0036	0.0020	0.0018	0.0050	0.0052	0.0015	0.0019	0.0042	0.0067	0.0011	0.0013	0.0738	0.0706

ICP-MS	NB2a		NB8		NB10		NB10b		NB15		NB22		NB24		NB25		NB28	
ppm	run1	run2	run1	run2	run1	run2	run1	run2	run1	run2	run1	run2	run1	run2	run1	run2	run1	run2
Li	1.10	1.03	1.37	1.29	0.120	0.102	0.772	0.658	0.385	0.365	1.64	1.53	0.231	0.332	0.449	0.533	0.728	0.546
Be				0.0147					0.0208	0.0225							0.0394	0.0287
Al(M)		3974		7509		3910		8029		3794		4413		4888		4818		6680
P(M)	12.0	12.5	6.20	5.89	3.64	3.42	5.88	5.46	21.4	23.0	20.0	18.0	9.44	9.05	12.0	11.5	27.3	25.8
K(M)					67.1				49.0								167	
Ca(M)					282				1309								204	
Sc(M)	9.63	9.84	12.0	11.3	10.2	9.22	14.1	12.6	8.08	8.30	11.8	11.2	9.51	8.71	11.5	11.1	9.50	9.46
Ti(M)	75.7	77.1	163	152	81.6	71.8	234	217	46.3	46.9	133	124	143	129	144	133	123	114
V(M)	41.6	38.8	53.9	46.4	42.2	35.8	57.4	49.0	42.7	41.0	54.5	47.8	41.7	35.1	51.1	45.4	49.6	45.3
Mn(M)	1162	1045	1208	1040	829	711	799	737	893	869	1566	1434	832	708	991	865	2466	2325
Fe(M)	60560	58060	70340	63730	57030	49680	56490	53210	79900	80380	64290	59830	63150	55480	52190	46200	32370	31730
Co(M)	122	110	134	118	109	95.1	108	100.0	126	120	125	112	125	105	112	96.2	149	141
Ni(M)	2284	2380	7427	7352	2356	2365	2761	2975	3000	3300	2368	2434	2486	2448	2154	2175	3230	3517
Cu(M)	4.96	5.78	2.88	4.37			6.95	14.8	10.3	10.2	2.11	4.10	18.9	18.5	16.3	15.4	1.73	0.607
Zn(M)	55.8	45.1	52.4	60.5	49.0	41.6	47.4	22.9	52.9	57.6	181	68.0	42.6	45.7	40.9	49.4	75.7	68.0
Ga	0.877	1.09	1.13	1.29	0.753	0.879	1.39	1.62	0.794	1.03	0.576	0.729	0.950	1.06	0.940	1.16	1.43	1.57
Rb	0.176	0.197	0.657	0.703	0.158	0.151	0.0898	0.0970	0.0264	0.0378	0.256	0.347	0.183	0.191	0.105	0.115	1.58	1.57
Sr	0.990	1.04	2.34	2.11	0.427	0.358	1.02	0.993	0.415	0.462	1.08	1.07	0.493	0.484	0.679	0.739	3.90	3.61
Y	0.169	0.186	8.08	8.68	0.326	0.325	1.13	1.17	0.160	0.170	0.666	0.714	0.458	0.466	0.736	0.806	1.63	1.63
Zr	0.424	0.386	0.439	0.348	0.377	0.295	0.624	0.492	0.957	0.978	0.410	0.428	0.501	0.405	0.427	0.475	1.59	0.768
Nb	0.0253	0.0497	0.0176	0.0457	0.0194	0.0437	0.0219	0.0510	0.0605	0.0890	0.0232	0.0501	0.0272	0.0494	0.0148	0.0596	0.107	0.0778
Cs	0.0194	0.0200	0.0957	0.0933	0.0148	0.0150	0.0125	0.0124	0.0037	0.0046	0.0223	0.0225	0.0211	0.0193	0.0108	0.0104	0.145	0.140
Ba	1.74	1.66	15.7	14.9	4.28	3.53	1.39	1.32	5.50	5.19	5.27	5.13	6.09	4.49	3.49	3.33	136	114
La	0.0212	0.0250	4.08	4.14		0.0060	0.0152	0.0173	0.195	0.200	0.0524	0.0591	0.0199	0.0216	0.0327	0.0354	2.85	2.67
Ce	0.0354	0.0405	0.0763	0.0827		0.0121	0.0207	0.0218	0.506	0.512	0.110	0.116	0.0318	0.0300	0.0202	0.0274	1.80	1.57
Pr	0.0038	0.0042	0.780	0.801		0.0015	0.0043	0.0040	0.0399	0.0411	0.0119	0.0123	0.0054	0.0051	0.0042	0.0043	0.371	0.346
Nd	0.0149	0.0170	2.92	3.10	0.0079	0.0110	0.0338	0.0362	0.120	0.131	0.0511	0.0548	0.0311	0.0317	0.0291	0.0309	1.17	1.14
Sm	0.0047	0.0057	0.509	0.533	0.0067	0.0070	0.0315	0.0345	0.0170	0.0183	0.0203	0.0222	0.0188	0.0177	0.0202	0.0197	0.127	0.125
Eu	0.0025	0.0063	0.133	0.153	0.0050	0.0128	0.0087	0.0105	0.0071	0.0194	0.0093	0.0213	0.0092	0.0186	0.0096	0.0164	0.109	0.385
Tb	0.0020	0.0010	0.103	0.113	0.0029	0.0014	0.0162	0.0063	0.0030	0.0043	0.0093	0.0045	0.0072	0.0030	0.0103	0.0041	0.0278	0.0368
Gd	0.0089	0.0054	0.719	0.752	0.0126	0.0061	0.0698	0.0256	0.0211	0.0293	0.0404	0.0205	0.0339	0.0139	0.0447	0.0177	0.201	0.250
Dy	0.0180	0.0104	0.613	0.657	0.0297	0.0174	0.139	0.0745	0.0201	0.0244	0.0784	0.0466	0.0589	0.0294	0.0889	0.0459	0.148	0.192
Ho	0.0059	0.0061	0.148	0.161	0.0108	0.0115	0.0414	0.0452	0.0046	0.0053	0.0237	0.0261	0.0169	0.0164	0.0267	0.0281	0.0276	0.0286
Er	0.0219	0.0241	0.424	0.471	0.0389	0.0439	0.136	0.155	0.0167	0.0200	0.0825	0.0960	0.0558	0.0538	0.0926	0.0975	0.0790	0.0804
Tm	0.0042	0.0046	0.0561	0.0622	0.0069	0.0080	0.0221	0.0252	0.0030	0.0037	0.0143	0.0167	0.0095	0.0088	0.0157	0.0165	0.0108	0.0121
Yb	0.0311	0.0243	0.311	0.319	0.0460	0.0399	0.134	0.119	0.0235	0.0214	0.0967	0.0811	0.0602	0.0449	0.103	0.0802	0.0683	0.0685
Lu	0.0064	0.0044	0.0535	0.0471	0.0087	0.0065	0.0216	0.0174	0.0048	0.0037	0.0174	0.0128	0.0109	0.0073	0.0183	0.0125	0.0109	0.0097
Hf	0.0041	0.0053	0.0211	0.0516	0.0041	0.0065	0.0275	0.0346	0.0185	0.0207	0.0089	0.0140	0.0144	0.0150	0.0139	0.0179	0.0364	0.0251
Ta		0.0012		0.0080		0.0011	0.0008	0.0026	0.0064	0.0089	0.0010	0.0019	0.0015	0.0017	0.0010	0.0019	0.0052	0.0032
Tl	0.0014	0.0028	0.0085	0.0174	0.0030	0.0030	0.0016	0.0039	0.0092	0.0111	0.0046	0.0074	0.0060	0.0109	0.0095	0.0195	0.0921	0.0906
Pb	0.126	0.225	0.142	0.209		0.102	0.310	0.458		0.779	1.42	1.96	0.281	0.293	0.361	0.417		1.01
Th	0.0053	0.0058	0.0016	0.0019		0.0014	0.0025	0.0024	0.0549	0.0576	0.0137	0.0137	0.0045	0.0043	0.0029	0.0028	0.0800	0.0480
U	0.0032	0.0031	0.0025	0.0022	0.0010	0.0008	0.0018	0.0016	0.0525	0.0528	0.0059	0.0063	0.0097	0.0090	0.0019	0.0020	0.0218	0.0181

M donates measurements done in medium resolution, all others done in low resolution; run1 and run2 refer to separate dissolutions.
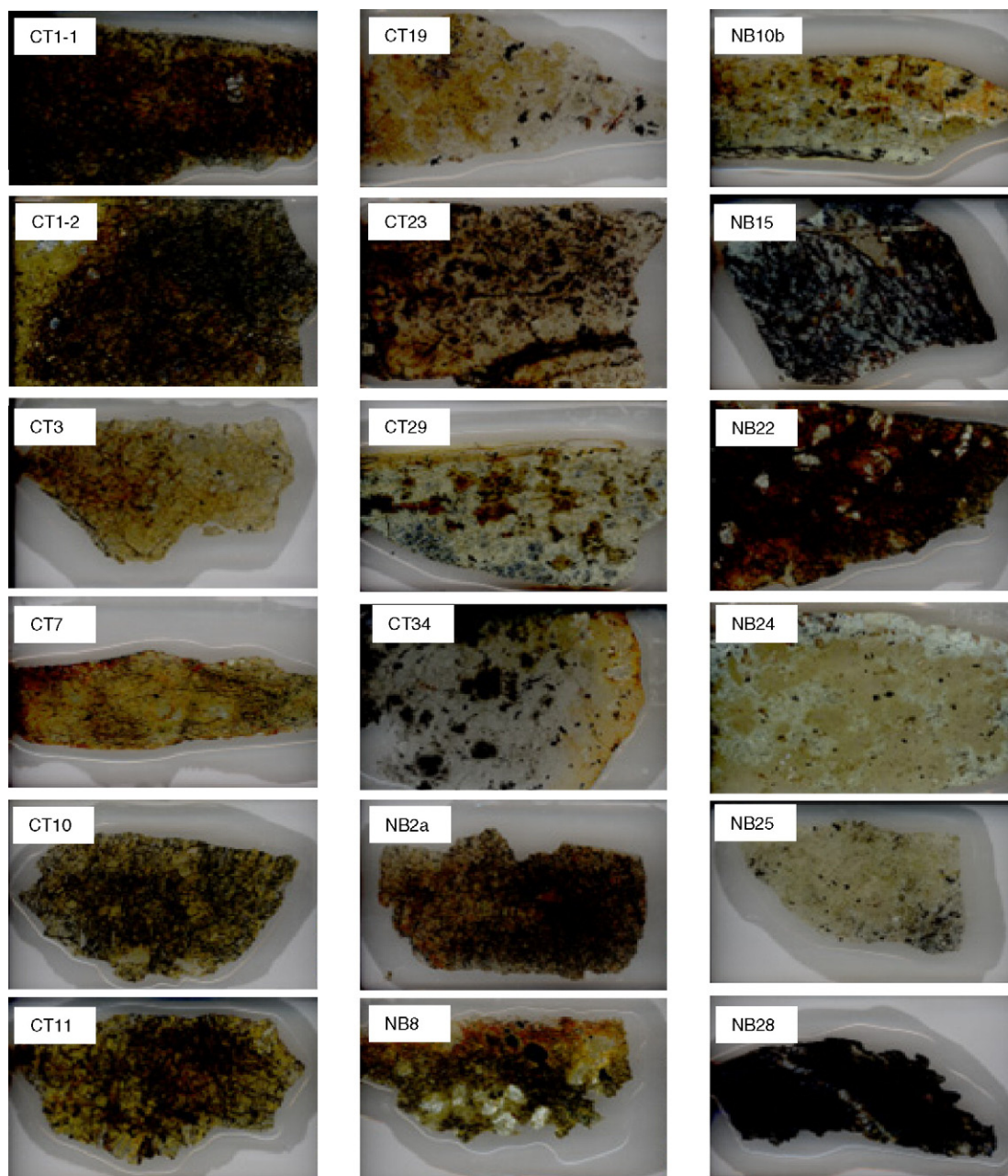
Appendix Fig. 1. Scanned petrographic thin sections of FRO peridotites. Sample NB10 is not shown.

conversion of the fayalite and ferrosilite components of olivines and pyroxenes, respectively, to magnetite.

Although all samples are extensively serpentinized, the nature of serpentinization varies. In many samples, the olivines and pyroxenes, although serpentinized, retain some relict features of their unserpentinized protolith. For example, serpentinized pyroxenes retain their angular shape and exsolution lamellae, while serpentinized olivines crudely retain their grain boundary morphologies. In such samples, fresh unserpentinized olivines and pyroxenes are occasionally found. Clinopyroxenes appear to be less easily serpentinized. Electron microprobe data (to be published elsewhere) on these minerals indicate olivine forsterite contents ranging from 0.89 to 0.915 and clinopyroxenes containing CaO contents ranging from 19 to 23.5 wt.% and Al_2O_3 contents ranging from 0.9 to 3 wt.%. These compositions are typical of primary peridotitic minerals; metamorphic diopsides associated with

rodingitization would be characterized by much lower Al_2O_3 contents (Hacker and Peacock, 1990). Original spinels appear not to be strongly affected by serpentinization. They are distinguished from secondary magnetite by their larger sizes, rounder shapes, and dark amber to opaque coloration. Such colors are due to their high Cr contents, which are consistent with their primary origins.

A smaller subset of samples (CT34, NB15, NB8 and NB28) includes those that are so serpentinized that there no longer exists any textural evidence of the primary silicate minerals. In hand specimen, these samples appear very dark (in contrast to the lighter green color of the less serpentinized samples), which we attribute to the conversion of all olivines and pyroxenes to serpentine plus magnetite, the latter giving the dark coloration. In such samples, even the original spinels appear to have been slightly affected as they appear to have partially recrystallized or broken down on their rims. These highly serpentinized samples come mostly from thin serpentine veins (several to ∼ 20 centimeter thick) cross-cutting the serpentinized peridotite bodies that show relict peridotite texture; they may thus represent a second generation of serpentinization. They will also be shown to have trace-element systematics fundamentally different from the rest of the samples.

The dominant serpentine mineral in these samples is lizardite/chrysotile. This is based on the fibrous and feathery texture of most of the serpentine in these samples. This interpretation is consistent with that of Mayfield and Day (2000) for much of the FRO, including the Sugar Pine Reservoir area. Importantly, the presence of lizardite/chrysotile as the dominant serpentine minerals indicates that the serpentinization temperatures for FRO peridotites were not higher than ∼ 300–400 °C (Evans, 1977; Evans, 2004). We cannot completely rule out that small amounts of antigorite, a more platy and higher temperature form of serpentine (<600 °C), are present in the field area. However, the absence of anthophyllite and talc (O'Hanley and Wicks, 1995; O'Hanley, 1996) is consistent with these low temperatures. We conclude that serpentinization in the Sugar Pine Reservoir area mostly occurred at greenschist facies conditions or lower (∼ <450 °C). This is lower than the peak metamorphic temperatures (>550 °C) reported by Hacker and Peacock (1990) in outcrops further to the north, but consistent with interpretations of Mayfield and Day (2000) in the Sugar Pine Reservoir area.

4.2. Whole-rock chemistry

4.2.1. Major and minor elements

Major, minor and trace element compositions measured by XRF and/or ICP-MS for all 19 samples are listed in Tables 1 and 2. The Mg#s (molar Mg/(Mg+Fe*), where Fe* represents total Fe), and concentrations of selected major elements (Si, Mg, Fe, Al and Cr) as well as transition elements (Mn, Ni and Ti) are plotted in Fig. 2A–I. We have also superimposed on Fig. 2A–I data from 1) spinel facies peridotite xenoliths compiled from the literature and 2) highly serpentinized abyssal peridotites dredged from the seafloor. The latter are taken from the data of Snow and Dick (1995) and have undergone extensive serpentinization associated with marine weathering. The former represents fragments of Phanerozoic subcontinental lithospheric mantle, which were sampled by entrainment in volcanoes. The xenoliths are simply used as a reference for unserpentinized mantle for major and selected minor and trace elements. We are well aware that mantle xenoliths have had complicated metasomatic histories, which could have altered their bulk compositions, particularly in the case of highly incompatible elements. However, for major elements and mildly incompatible elements (heavy rare-earths, Y, Sc, Al, Mn, and Fe), these xenoliths retain their original melting systematics because such elements are not significantly modified by metasomatic processes (Canil, 2004). We are further motivated to use xenoliths as references for unserpentinized mantle because we wish to avoid having to reconstruct model protolith compositions from highly serpentinized peridotites—a process in which high uncertainties in mineral mode estimates are unavoidable. The xenoliths chosen show little or no serpentinization and therefore provide a reference for pristine, unserpentinized mantle. A model composition of primitive mantle is also shown for reference (McDonough and Sun, 1995).

We have chosen to normalize compositional data to Cr_2O_3 in Fig. 2B–I in order to eliminate dilution effects caused by hydration during serpentinization. Normalization to an element also eliminates analytical artifacts associated with low totals from XRF. The best normalization element is one that is relatively immobile during serpentinization, that is, it is neither lost nor gained during serpentinization. Elements such as Mg, Ca, Ni, and Si are known to be mobile during metamorphism or weathering. Chromium, however, is relatively immobile, and this is borne out by the fact that, in thin section, primary Cr-spinel grains are usually preserved in the serpentinized FRO rocks. Cr is also a compatible element during melting and therefore its absolute abundance in a peridotite, regardless of the degree of weathering, should remain relatively constant. It is for these reasons, we have chosen Cr as a normalizing element. We recognize that although Al is probably also fairly immobile during aqueous processes, its high
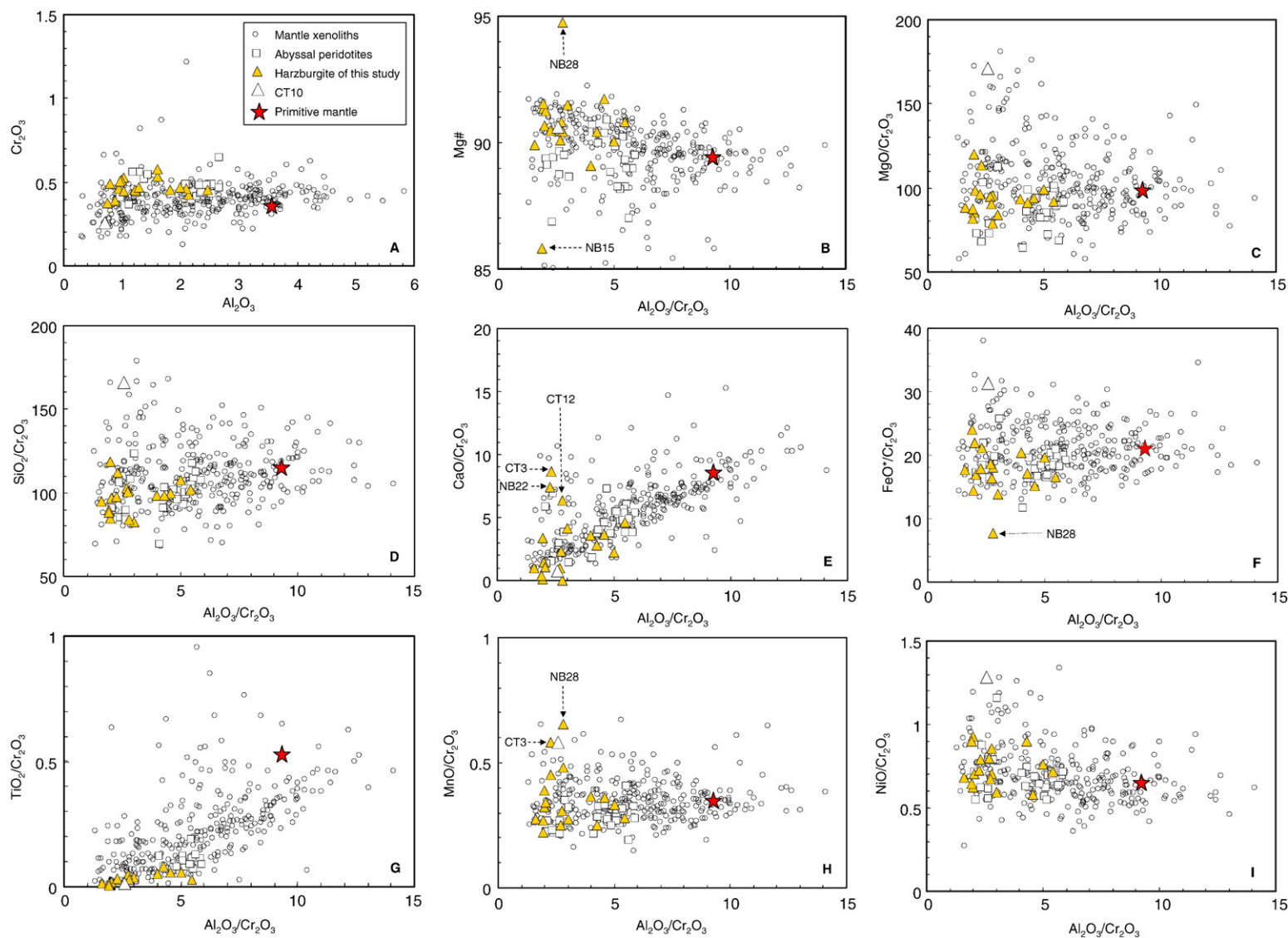
Fig. 2. Cr_2O_3 normalized major and minor element whole-rock compositions of Feather River Ophiolite (FRO) peridotites (filled triangles). Mg# (b) corresponds to molar Mg/(Mg+Fe*) where Fe* is taken as total Fe. Also shown are literature data for mantle xenoliths (open circles) and abyssal peridotites (open squares; (Snow and Dick, 1995)). Primitive Mantle composition (McDonough and Sun, 1995) is shown for reference (star). Names of outliers have been labeled. CT10 is denoted with an open triangle due to its anomalously low Cr content, which causes it to be an outlier in all plots.

intrinsic variability in mantle rocks (due to its incompatible behavior during melting and the possibility of varying degrees of melt depletion) would result in very large spreads in ratios with Al_2O_3 as a denominator, such that geochemical correlations associated with melting processes would be magnified, masking secondary (e.g. post-melting) element mobilization associated with serpentinization. There are, nevertheless, drawbacks of using Cr_2O_3 as a normalizing element. First, the analytical precision for Cr_2O_3 may not be as good as Al_2O_3. This may explain some of the scatter in Fig. 2, particularly in the xenolith data set, which includes analyses from different laboratories. Second, the use of Cr may be complicated by the presence of podiform chromitites, which are known to occur in ophiolite bodies. However, none of our samples have unusually high Cr contents. In addition, our samples do not show layers or accumulations of rounded chromite as would be expected for podiform chromitites. Finally, a large component of podiform chromitites would result in data arrays trending towards the origin on a plot of SiO_2/Cr_2O_3 versus Al_2O_3/Cr_2O_3 (Fig. 2D).

While Al_2O_3 is not a good normalizing element because it varies with melt depletion, it is exactly this property combined with its relative immobility that makes the Al_2O_3/Cr_2O_3 ratio a good proxy for melt depletion (Fig. 2B–I): Al is incompatible and Cr moderately compatible in the residue during melting, hence their ratio decreases with increasing melt extraction. Two important features stand out in Fig. 2A–I. First, the serpentinized peridotites appear to preserve elemental systematics imparted by partial melt extraction. For example, increasing melt extraction (decreasing Al_2O_3/Cr_2O_3) leaves behind olivine-rich and pyroxene-poor residues (e.g., dunites and harzburgites) having low Al_2O_3, CaO and TiO_2, high Mg# (molar $Mg/(Mg+total\ Fe) \times 100$) and NiO, relatively constant FeO, MnO, Cr_2O_3 and slightly lower SiO_2. These features can be seen in both the unserpentinized xenolith samples and the serpentinitized FRO peridotites. For the most part, it can be seen that most of the FRO peridotites appear to have experienced high degrees of melting as exemplified by their low Al_2O_3/Cr_2O_3 ratios (<5) and their high Mg#s (mostly greater than 90). For reference, fertile mantle has Al_2O_3/Cr_2O_3 ratio of ~14 and an Mg# of ~89 (McDonough and Sun, 1995).

It can also be seen from Fig. 2 that the Cr_2O_3-normalized major and minor element systematics (except for Na and K, which are not shown) in most of the serpentinized FRO peridotites are indistinguishable from those of the peridotite xenoliths, which are unserpentinized. There are, however, a few exceptions. Sample

CT10 has extremely low Cr content, resulting in its high Cr_2O_3-normalized MgO, SiO_2, FeO*, MnO and NiO contents. Three samples show anomalously high CaO/Cr_2O_3. Two samples (excluding CT10) show slightly high MnO/Cr_2O_3. Finally, two samples show anomalous Mg#s: NB28, a highly serpentinized sample showing no relict peridotite textures, is characterized by high Mg# due to low FeO contents; NB15, another highly serpentinized sample showing no relict textures, is characterized by low Mg#.

In Fig. 2A–I, we can also compare our samples to abyssal peridotites dredged from the seafloor. These samples have been exposed to extremely high water–rock ratios because they have been exposed at the base of the ocean for millions of years. It has been shown that abyssal peridotites have experienced extensive Mg loss (Snow and Dick, 1995). This can be seen in our figures: although most major element systematics in abyssal peridotites (Snow and Dick, 1995) have remained relatively undisturbed, they are characterized by anomalously low MgO/Cr_2O_3 contents and low Mg#s, which collectively indicate preferential Mg loss. This loss of Mg contrasts with the relatively undisturbed Mg of the majority of the FRO peridotites (Fig. 2B, C).

We conclude from this section that, with few exceptions, serpentinization of FRO peridotites was not accompanied by significant mass change besides the addition of the water needed for serpentinization.

4.2.2. Trace elements

Trace element compositions normalized to primitive mantle values (McDonough and Sun, 1995) are presented in Fig. 3. Samples CT34, NB8, NB15 and NB28 were specifically identified because of their unusual trace-element signatures; these samples, as discussed above, represent thin highly serpentinized cross-cutting veins. The remaining samples, which we show in Fig. 3A, have very similar trace-element abundance patterns and are herein referred to as the "normal" samples. The four anomalous samples are shown in Fig. 3B and C along with the average of the samples in Fig. 3A. The elements plotted in Fig. 3 are in approximate order of increasing compatibility in silicate minerals within basaltic systems.

The normal FRO peridotites are distinguished from the four anomalous samples in that they have overall positive-sloped rare-earth element (REE) patterns due to the depletion in light REEs (LREE) compared to the heavy REEs (HREE). In contrast, the four anomalous samples all have negatively sloped REE patterns associated with enrichment of LREEs relative to the HREEs. These four anomalous samples differ amongst
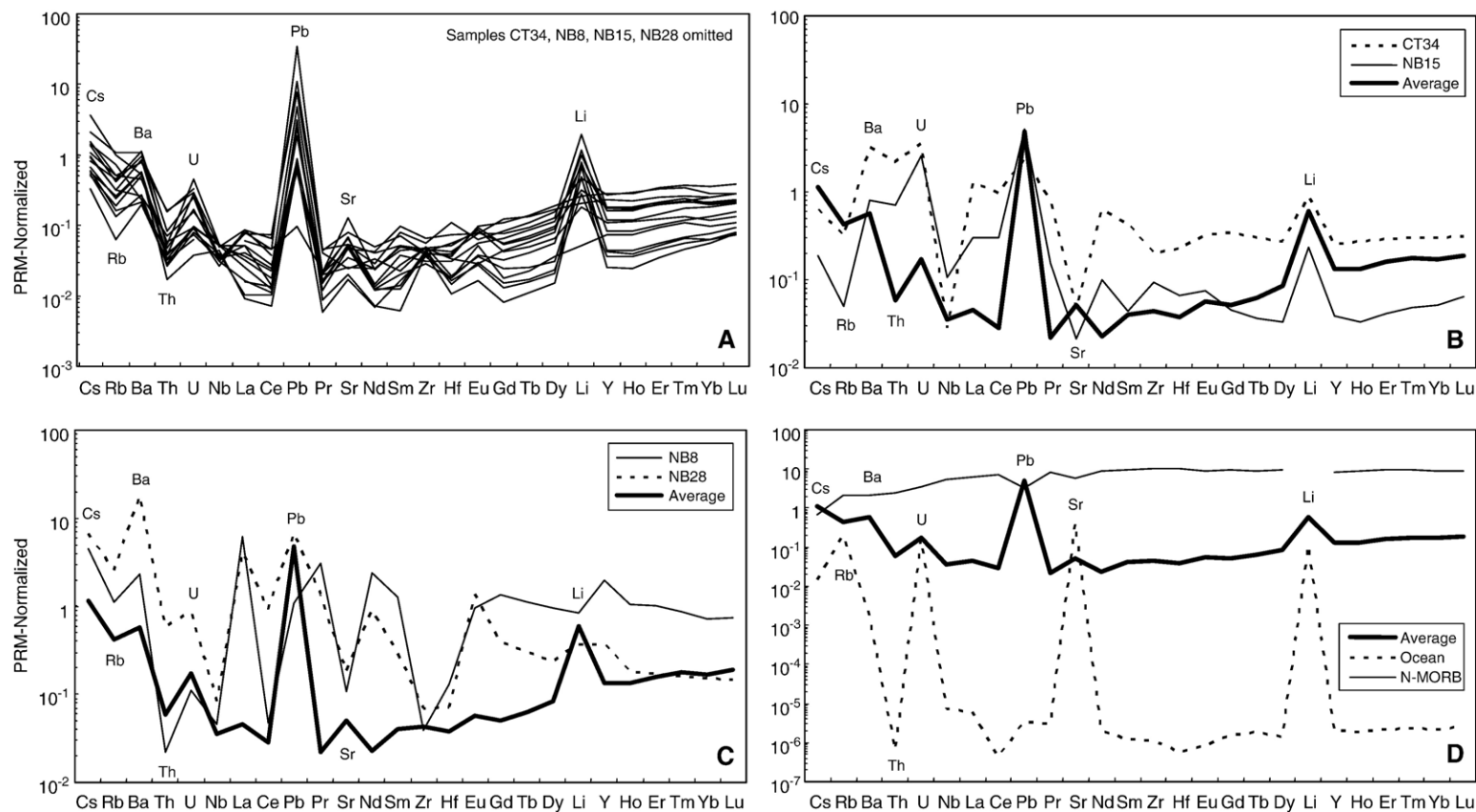
Fig. 3. Primitive mantle normalized trace element compositions of FRO peridotites. A: compositions of normal FRO peridotites; B: compositions of samples CT34 and NB15 together with the average compositions of normal FRO peridotites in A; C: compositions of samples NB8 and NB28 together with the average compositions of normal FRO peridotites in A; D: comparison of the average trace element composition of normal FRO peridotites in A to N-MORB and global seawater compositions.

themselves by the fact that two samples (NB8 and NB28; Fig. 3C) have negative Ce anomalies and two other samples (CT34 and NB15; Fig. 3B) have no Ce anomalies. All 19 samples are characterized by variable enrichments in the large ion lithophile elements. In the case of the normal samples, the large ion lithophile elements, Cs, Rb, Ba, U, Pb, Sr and Li are all highly enriched. The anomalous samples are also enriched in some of these elements, but there appears to be no enrichment in Sr, resulting in extreme negative Sr anomalies relative to the REEs. The four anomalous samples also show little or no enrichments in high field strength elements (Nb, Ta, Zr, Hf and Ti) and otherwise have high field strength element abundances identical to or only slightly higher than in the normal samples. However, because the anomalous samples are La-enriched, they are characterized by very low Nb/La ratios, whereas the normal samples have more chondritic Nb/La ratios. Finally, we note that all 19 samples have very high Pb contents (Fig. 3A–C) and thus low Ce/Pb ratios (~<6). We will discuss the origin of these trace-element abundance patterns in Section 5.

5. Discussion

5.1. Origin of serpentinization

5.1.1. An in situ origin for serpentinization

Fig. 4 shows cartoons of possible serpentinization mechanisms for peridotites from oceanic lithospheric mantle. Serpentinization can occur by A) infiltration of seawater into oceanic lithosphere via oceanic fractures, B) marine weathering of peridotite that has been exhumed to the surface at fracture zones or low-angle detachment faults, C) infiltration of seawater into extensional faults formed in the bend of a subducting slab, or D) dehydration of subducting or underthrusting oceanic crust followed by fluid fluxing of overlying mantle wedge material. We describe serpentinization via scenario B as an *ex situ* process, whereas all other processes are *in situ* processes, that is, serpentinization of the peridotites occurred largely in place within the oceanic lithospheric mantle or mantle wedge. Scenario B further differs in that the integrated water–rock ratio during marine weathering of exhumed peridotites is extremely large. As pointed out earlier, a fundamental feature of marine weathering serpentinization is that there is significant Mg loss due to the under-saturated nature of Mg in seawater (Snow and Dick, 1995). In contrast, the water–rock ratio in the three other processes (A, C, D) is likely to be much lower hence Mg-saturation in hydrothermal waters is likely to be reached fairly quickly in a semi-closed system environment. As a result, no significant Mg loss from peridotites will be expected. Indeed, the serpentinization process in many ophiolite sections has been shown to be largely isochemical, at least in terms of the major elements (Komor et al., 1985). The FRO peridotites for the most part appear to be isochemical. We realize, however, that it is possible for *ex situ* serpentinization (Scenario B,
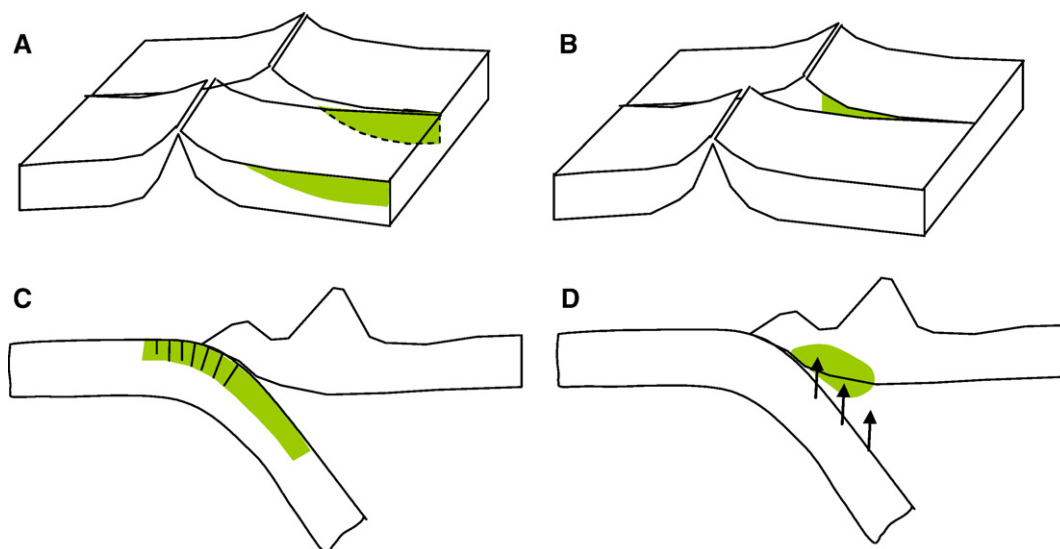

Fig. 4. Cartoons illustrating possible scenarios by which oceanic lithospheric mantle is serpentinized. A: infiltration of seawater into oceanic lithosphere via transform faults; B: marine weathering of peridotite that has been exhumed to the surface at fracture zones or low-angle detachment faults (abyssal peridotites); C: infiltration of seawater into extensional faults formed in the bend of a subducting slab; D: serpentinization of fore-arc mantle wedge material by fluids originating from subducting slab dehydration.

Fig. 4B) to occur without severe alteration (and thus no significant Mg loss) in individual cases. The most likely situation for this to happen is when the exposure time of peridotites on the seafloor is relatively short. We believe that it is unlikely (but not impossible) that FRO peridotites were serpentinized in this way as the majority of the FRO peridotites we collected were highly serpentinized (>90%). We thus interpret that serpentinization of the FRO peridotites was an *in situ* process (Fig. 4A, C, or D) and not the product of marine (or sub-aerial) weathering (Fig. 4B). In the future, however, a potential way of distinguishing serpentinization processes within different geologic settings comes from chlorine stable isotope study on serpentinites as suggested by a recent study of Barnes and Sharp (2006).

5.1.2. Two types of serpentinization processes

We now turn to the trace-element signatures of the FRO peridotites. As pointed out above, the normal FRO peridotites are characterized by enrichments in fluid-mobile elements (LILEs) Cs, Rb, Ba, U, Sr and Li (Fig. 3A). Because both seawater (Fig. 3D) and fluids released during dehydration of a subducting slab are enriched in these elements (Saunders et al., 1980; Gill, 1981; Pearce, 1983; Tatsumi, 1986; McCulloch and Gamble, 1991; Stolper and Newman, 1994; Brenan et al., 1995; Keppler, 1996; Kogiso et al., 1997; Stalder et al., 1998), the enrichment patterns of normal FRO peridotites can be explained either by seawater-derived hydrothermal fluid infiltration or by slab dehydration-related fluid fluxing. If fluids released into the mantle wedge by subducting slabs are slightly hotter than that characterizing seawater infiltration into lithosphere, we might expect a slight enrichment in LREEs (e.g., La, Ce, Pr) relative to HFSEs (e.g., Ti, Nb, Zr and Hf). This is because at temperatures higher than only ~ 300 °C, small amounts of LREEs might be mobilized (Gammons et al., 1996) while HFSEs remain relatively insoluble in hydrous melts compared to the LREEs (Saunders et al., 1980; Gill, 1981; Pearce, 1983; Keppler, 1996). As a result, chemical transport by such fluids will generate both LILE and LREE enrichments and apparent depletions in HFSEs. The overall LREE depleted signatures (compared to HFSEs) of the normal FRO peridotites indicate that subduction-related fluids were probably not responsible for most of the serpentinization seen in the FRO unless the temperatures of these fluids were very low. Thus, based on the seawater signature, conservation of major element compositions (Fig. 2) and low metamorphic temperatures, our preferred interpretation is that the majority of the FRO peridotites were serpentinized by seawater while they were structurally in place within the oceanic lithosphere, and thus not during or after tectonic obduction. We speculate that the FRO peridotites were probably serpentinized via fractures or faults in the lithosphere, e.g. Fig. 4A and C.

The four anomalous samples, however, show selective enrichments in LREEs relative to HREEs, a feature that cannot be imparted by the addition of seawater alone because seawater is depleted in REEs. Importantly, because these four samples do not show enrichments in the HFSEs, the enrichments in La result in low Nb/La ratios. The enrichment in LREEs suggests that the parental fluids responsible for these anomalous samples were probably of higher temperature origin than those responsible for the rest of the FRO peridotites. A peculiar feature of these four anomalous samples is that one group (NB8 and NB28) has both Ce and Sr depletions and another (CT34 and NB15) has only Sr depletions. In addition to be slightly hotter, these observations lead us to speculate that they may have pre-reacted with plagioclase within a gabbro layer. Our reasoning is based on the following. Plagioclase preferentially holds back Sr (to substitute for Ca^{2+}) so co-existing fluids will be depleted in Sr. In order to fractionate Ce from neighboring REEs, La and Pr, Ce must be oxidized from the +3 state typical of the REEs to the +4 state. It is much easier to oxidize Ce to its +4 state than to oxidize La and Pr. Because Ce^{+4} is much more insoluble than Ce^{+3} and other REEs in their +3 state, it is likely to be depleted in hydrothermal fluids. We note that in oxidative environments, some of the Eu in plagioclase would be oxidized from its +2 state to the +3 state. Plagioclase is highly enriched in Eu^{2+}, but because Eu^{3+} does not partition in to plagioclase, oxidation of Eu would result in liberation of Eu into hydrothermal fluids. This may explain the positive Eu anomalies in some of the anomalous samples. We conclude that samples NB8 and NB28 were serpentinized by oxidative fluids pre-reacted with gabbro, while samples CT34 and NB15 were serpentinized by similarly pre-reacted fluids, but at less oxidative conditions.

In conclusion, in the Sugar Pine Reservoir area, it appears that there are two groups of serpentinites, a dominant group that preserves the original imprint of hydrothermal serpentinization of the oceanic lithosphere by seawater and another group, manifested primarily by small cross-cutting veins (see Section 4.1), that evoke a second-stage serpentinization imprint by fluids which might have previously reacted with plagioclase in a gabbro layer. This second-stage serpentinization imprint could have been associated with the tectonic obduction and exhumation of these serpentinites, and if so, would be consistent with similar suggestions for the northern

FRO and the Trinity ophiolite further north (Hacker and Peacock, 1990). In the Sugar Pine Reservoir area, however, original seawater-related hydrothermal serpentinization has been largely preserved, suggesting that, on average, the metamorphic grade in this region was lower than to the north. Of concern here are the normal FRO peridotites, which preserve this original serpentinization imprint. These samples are most relevant for understanding the mechanism and extent of *in situ* serpentinization of oceanic lithosphere.

5.1.3. A note on the large positive Pb anomalies

One enrichment feature that is not, at face value, consistent with a seawater signature is the high Pb concentrations in all FRO samples, resulting in low Ce/Pb ratios. Cerium and Lead are both moderately incompatible and behave similarly during magmatic processes, so partial melting and/or mantle metasomatism cannot explain the low Ce/Pb ratios. However, Ce/Pb ratios can be fractionated during aqueous fluid-related processes as the aqueous solubility of Pb is much greater than that of Ce (You et al., 1996). Seawater-derived hydrothermal fluids may travel through oceanic sediments and basaltic crust, and in so doing, may preferentially extract Pb relative to Ce from wallrock. Infiltration of these Pb-enriched fluids into peridotites could generate low Ce/Pb ratios during serpentinization.

5.2. Melting degrees

Now that we have argued that the FRO probably represents oceanic lithospheric mantle that was serpentinized in place beneath the seafloor, we move one step closer to our goal of quantifying the recycling rate of water via subduction zones. A key step is to constrain the depth to which serpentinization occurred. If we can constrain the paleo-depths of the FRO peridotites within the oceanic lithospheric mantle from which they are inferred to have originated, we can make a crude estimate of the vertical extent of lithospheric serpentinization. We make the bold assumption that because serpentinization was in situ and hence pre-dates tectonic obduction/exhumation, the paleo-depths of the peridotites represent the serpentinization depths. This assumption is predicated on additional assumptions: 1) FRO represents an obducted normal oceanic lithospheric mantle section, 2) mantle melting occurs in a passive adiabatically upwelling regime beneath mid-ocean ridges, 3) the depth at which the peridotites last melted corresponds roughly to their average paleo-depths within the oceanic lithosphere (in other words, asthenospheric mantle rising from beneath travels horizontally away from the mid-ocean

ridge at a roughly constant depth after the last-stage of melting) and 4) serpentinization predates any tectonic thinning or thickening associated with obduction of the ophiolite. The last assumption is justified insofar as we have correctly interpreted that the peridotites were serpentinized by seawater while structurally in place within the oceanic lithosphere prior to tectonic accretion. Estimates of the melting degree F coupled with a relationship between F, depth, and mantle potential temperature then allow us to roughly constrain the average depth at which melt was last extracted from these peridotites. This section concerns how we estimate F.

We have attempted to estimate F from major and trace elements. We used the pMELTs thermodynamic model (Ghiorso and Sack, 1995; Asimow and Ghiorso, 1998) to quantify the relationship between F and MgO during partial melting of a lherzolite having a roughly pyrolitic major element composition (McDonough and Sun, 1995). We assumed, for simplicity, isobaric anhydrous batch melting. For the crude estimates of F that we are seeking, this simplifying assumption is not a serious problem. MgO-based estimates (MgO contents were normalized to an anhydrous basis) of melting degree are shown in Fig. 5 and Table 1 and range from ∼17 to 36.5%, averaging 26%. Similar estimates are obtained using experimentally-determined relationships (Niu, 1997; Herzberg, 2004).

We have also constructed a melting model for trace elements (see Appendix A for details). We assumed fractional and batch melting using a melting stoichiometry determined from pMELTs at 1.5 GPa and partition coefficients used in Niu and Hékinian (1997). Results are
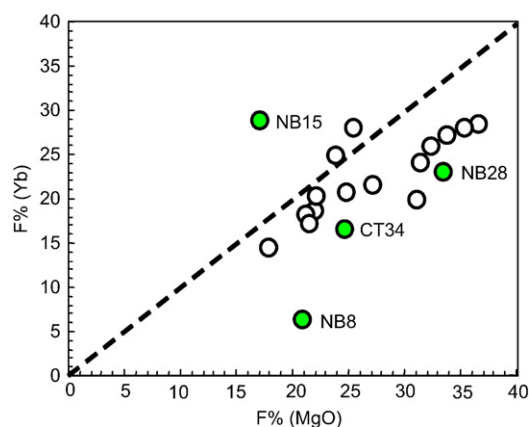

Fig. 5. Estimated melting fractions (F) of FRO peridotites based on their MgO contents versus that estimated based on their Yb contents (MgO and Yb were normalized to an anhydrous basis). The four samples (CT34, NB8, NB15 and NB28; Fig. 3b and c) which have anomalous trace-element signatures are distinguished from the normal FRO samples with different colors.
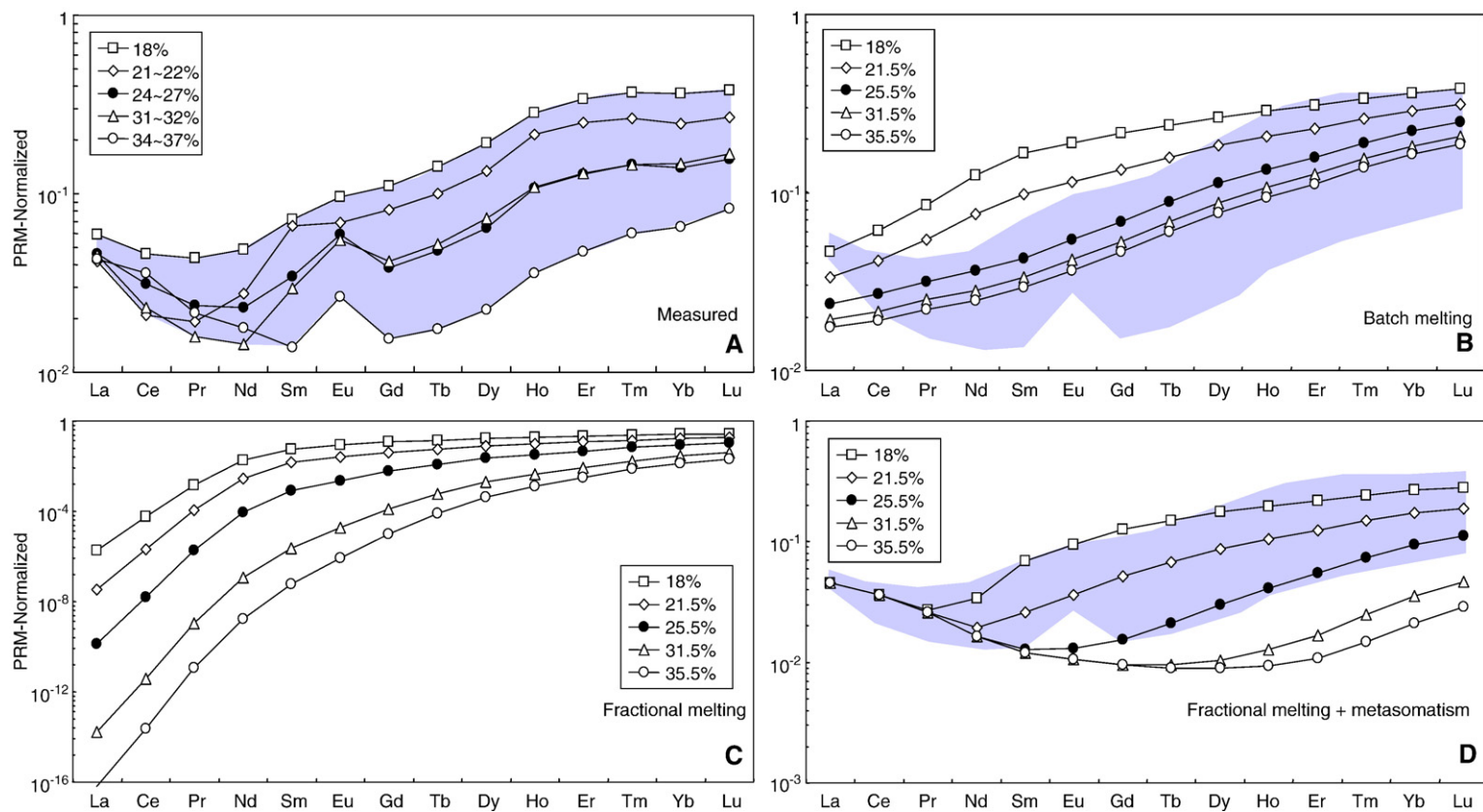
Fig. 6. Comparison between measured rare-earth element (REE) compositions of normal FRO peridotites and results from partial melting models. A: primitive mantle normalized REE compositions of normal FRO peridotites grouped in terms of intervals of melt fraction *F* as determined from MgO content (Fig. 5). B: calculated REE abundance patterns of peridotites that have undergone batch melting. Abundance patterns are calculated for melt fractions corresponding to those shown in A. Observed range in A has been superimposed in B for reference. C: calculated REE abundance patterns that have undergone fractional melt extraction. D: calculated REE compositions that have undergone fractional melt extraction followed by the addition of small amounts of a melt. Observed range in A was again superimposed here.

shown in Fig. 6. In Fig. 6A, we have categorized the normal FRO peridotites into F groups based on MgO content. Fig. 6B shows the results of batch melting superimposed on the REE diagrams of the FRO peridotites. It can be seen that batch melting fails to explain the low HREE abundances in the FRO peridotites. This is not surprising because it is generally believed that the more realistic melting process is fractional, which more efficiently depletes residues in incompatible elements (Johnson et al., 1990). Pure fractional melting (Fig. 6C), however, results in extreme LREE-depletion, which is not seen in the FRO peridotites. In Fig. 6D, we show that the REE patterns can be reconciled by a combination of fractional melting followed by the addition of a small degree melt that is enriched in LREEs (see Appendix A for details). Importantly, addition of a small amount of LREE-enriched melt can give the slight concave upward REE abundance pattern in the FRO peridotites because it significantly affects the LREEs but only minimally affects the HREEs (Fig. 6D). Because of the HREEs are less disturbed, their concentrations should reflect melting degree F much better than LREE concentrations.

For comparison (Fig. 5), we have plotted Fs estimated from the Yb depletions in the FRO peridotites versus F determined by MgO. There is a positive correlation between F_{Yb} and F_{MgO} as expected. Although F_{MgO} is systematically higher than F_{Yb} by about 5%, the small systematic difference could be due to the imperfect assumption of pure fractional melting or to slight Mg mobility. In all ensuing discussions, we will use the F determined by MgO content.

5.3. Paleo-depths

With the melting degrees F derived above, the paleo-depths and thus the approximate serpentinization depths for the normal FRO peridotites were calculated using an F-depth relationship derived from the anhydrous mantle melting model of Katz et al. (2003). Melting degree contours (F-contours) are shown in Fig. 7 for the range (~18–36%) and average (~27%) of inferred F_{MgO} in the previous section. We have also plotted various adiabatic melting paths following methods outlined in Katz et al. (2003). At mid-ocean ridges, mantle potential temperature estimates range from 1260–1280 °C (McKenzie and Bickle, 1988; Presnall et al., 2002) to 1410–1475 °C (Kinzler and Grove, 1992; Asimow et al., 2001). We took the average potential temperature to be ~1350 °C and melting paths for potential temperatures ranging from 1300 to 1400 °C were calculated. The intersection of the melting adiabat with an F_{MgO} contour represents a crude estimate of the paleo-pressure at
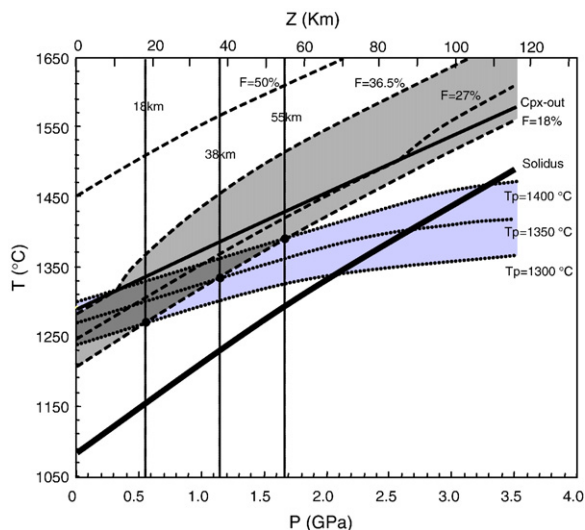

Fig. 7. Paleo-depths of FRO peridotites assuming passive upwelling system and using an anhydrous mantle melting model (Katz et al., 2003). Intersection of melting adiabat (for mantle potential temperatures ranging from 1300 to 1400 °C) with the average melting degree recorded by the FRO peridotites represents the average pressure of melt extraction. Minimum, average, and maximum melting degrees (18, 27, and 36.5 wt.%) determined from MgO contents are labeled. The curve labeled as "Cpx-out" denotes the point at which clinopyroxene is exhausted in the solid residue as melting proceeds.

which the normal FRO peridotites melted. It is obvious from Fig. 7 that for a given mantle potential temperature, higher degree melt residues (e.g., high F_{MgO}) imply shallower final depths of melt extraction whereas lower degree melt residues imply greater depths. Similarly, if a high mantle potential temperature is assumed, a higher melt extraction depth would be obtained for a given F_{MgO}.

Taking the average normal mantle potential temperature to be 1350 °C, we find a paleo-depth of ~15 km for an average F_{MgO} of ~27%. However, it is unlikely that the entire melting column is represented in the FRO. It is more likely that only the uppermost part of the oceanic lithosphere is preserved during obduction. As melting degree F_{MgO} of melt residues decreases with depth along given mantle melting path (Fig. 7), the paleo-depth represented by the FRO samples of the smallest melting degree F_{MgO} (18%) provides the minimum bound on the depth extent of the oceanic lithosphere that is presently sampled by FRO. For a potential temperature of 1350 °C, this yields a depth of ~40 km. Because all of the FRO peridotites are serpentinized, this implies that serpentinization of the lithospheric mantle extended at least to ~40 km.

Half-space cooling calculation indicates the temperature at ~40 km for oceanic lithospheres of ~75 Ma (the average age of subducting oceanic lithosphere) is

∼550 °C yet the maximum temperatures reached in the FRO peridotites, based on the presence of chrysotile/lizardite, is ∼300–400 °C (Evans, 1977; Evans, 2004). For younger oceanic lithosphere, the temperature discrepancy is even bigger. This indicates that either our serpentinization depth (∼40 km) has been overestimated, or the lithospheric mantle around fractures tends to be more efficiently cooled by mechanisms which cannot be described by half-space cooling alone. The possibility of overestimation is illustrated in Fig. 7 by the fact that 50 °C mantle potential temperature drop will reduce the estimated paleo-serpentinization depth for FRO peridotites to ∼20 km. In such case, no further cooling mechanism other than half-space cooling will be required.

As it is unclear whether the serpentiniztion depth has been overestimated or cooling mechanisms other than half-space cooling do exist in fracture vicinities, the 40 km estimate will be used in following discussions. We suggest, however, that caution should be taken when using our results for further interpretations or modeling constraints.

5.4. Speculations on water recycling rate

In this section, we speculate on the influence of serpentinization on subduction recycling of water. So far, most attempts to investigate recycling of water via serpentine subduction have assumed a hypothetical value for the extent of serpentinization in oceanic lithospheric mantle (Rüpke et al., 2004). As stated in the Introduction, observational constraints are few. The study of Ranero et al. (2003) suggested a minimum serpentinization depth of ∼20 km near the bending region of subducting slabs. The location of the double-seismic zone in subducting slabs suggests that serpentinization may reach ∼50 km into the slab (Hacker et al., 2003). Our observational constraints suggest that, at least for the FRO, serpentinization reached at least 40 km depth by taking the mantle potential temperature to be 1350 °C.

In order to explore the implications of serpentinization for water recycling, we assume that our constraints on the vertical extent of oceanic lithosphere serpentinization in the FRO is a general feature. We further assume that most of this serpentinization is associated with serpentinization "aureoles" around fractures that have penetrated into the lithospheric mantle. The width of these serpentinization aureoles is assumed to be limited by the rate at which water in the fracture diffuses into the wallrock and is hence time-dependent. The extent to which oceanic lithospheric mantle is serpentinized thus depends on the vertical and lateral extent of serpentiniza-

tion, the latter which depends on the number of fractures and thickness of serpentinized "aureoles".

5.4.1. Water recycling via serpentinized aureoles around fracture zones and faults

The number and width of serpentinization aureoles is treated by considering different fracture scenarios. One scenario is that illustrated in Fig. 4A. Here, infiltration of seawater into oceanic lithosphere occurs via transform faults intrinsic to the oceanic lithosphere prior to subduction. We assume that the depth to which seawater can extend into these transform faults is fixed by our estimated paleo-depths for the FRO peridotites (the paleo-depths as estimated from different melting models corresponding to 1300, 1350, and 1400 °C potential temperatures were considered). An order-of-magnitude estimate of the width of the serpentinized aureole was determined by estimating the diffusion lengthscale over the global average age of the oceanic lithosphere just prior to subduction. The rate at which serpentinization takes place is controlled by an effective diffusion coefficient of water through porous ultramafic media; this assumes that serpentinization reactions keep up with water infiltration (Macdonald and Fyfe, 1985). Table 3 shows the resulting global recycling rates estimated using the global trench length and average subduction rate of Bird (2003). Details of our calculations are given in the Appendix B. Taking our paleo-depth (∼40 km) estimates for the case in which the mantle potential temperature is 1350 °C, we find that subduction of serpentinized transform faults accounts for a global recycling rate of ∼1.6×10^{18} kg/Ma. For comparison, we have also estimated the probably unrealistic case in which the entire lateral extent of oceanic lithosphere is serpentinized down to its maximum serpentinization depth. This amounts to a maximum bound of water recycling of ∼5.5×10^{19} kg/Ma.

In a second scenario, illustrated in Fig. 4C, seawater enters trench-parallel normal faults that form at the bending zone just prior to subduction. We assume that these normal faults represent reactivated normal faults originally formed at spreading centers (Ranero et al., 2003). We adopt a trench-parallel fault density of 0.2 fractures/km, which is based on generalizing the observed baseline fracture density seen in the subduction bending zone at the middle American trench (Ranero et al., 2003) (see Appendix B for details). New faults undoubtedly form as the slab approaches the trench; for example, at the middle America trench, the fault density increases from the baseline value of 0.2 at the beginning of the bend to ∼1.8 just prior to subduction (Ranero et al., 2003). We ignore this increase in fault density within the bend of a subducting slab because the growth rate is not

Table 3
Lateral serpentinization extent and global water recycling extent

	Unit	Oceanic fractures (transform faults)	Extensive	Extensional faults (constant Z)	Extensional faults (linear Z)
H₂O recycling rate through lithospheric mantle (T_p=1300 °C, Z=18 km)[1]	kg/Ma	7.3×10^{17}	2.6×10^{19}	5.7×10^{18}	3.8×10^{18}
H₂O recycling rate through lithospheric mantle (T_p=1350 °C, Z=38 km)[1]	kg/Ma	1.6×10^{18}	5.5×10^{19}	1.2×10^{19}	8.0×10^{18}
H₂O recycling rate through lithospheric mantle (T_p=1400 °C, Z=55 km)[1]	kg/Ma	2.2×10^{18}	7.9×10^{19}	1.7×10^{19}	1.2×10^{19}
Mantle serpentinization extent S	wt.%	3	100	22	15
H₂O recycling rate through sediments[2]	kg/Ma	1.9×10^{17}	1.9×10^{17}	1.9×10^{17}	1.9×10^{17}
H₂O recycling rate through basaltic crust[3]	kg/Ma	5.4×10^{17}	5.4×10^{17}	5.4×10^{17}	5.4×10^{17}
Total H₂O recycling rate (T_p=1300 °C, Z=18 km)[4]	kg/Ma	1.5×10^{18}	2.7×10^{19}	6.4×10^{18}	4.5×10^{18}
Total H₂O recycling rate (T_p=1350 °C, Z=38 km)[4]	kg/Ma	2.3×10^{18}	5.6×10^{19}	1.3×10^{19}	8.7×10^{18}
Total H₂O recycling rate (T_p=1400 °C, Z=55 km)[4]	kg/Ma	3.0×10^{18}	8.0×10^{19}	1.8×10^{19}	1.3×10^{19}

1. T_p: normal mantle potential temperature; Z: serpentinization depth. The uncertainties in estimated H₂O recycling rate is ∼40%.
2. Global subducting sediment composition is after Plank and Langmuir (1998) and the thickness of sediment is taken to be 350 m.
3. The thickness and water content of hydrated oceanic crust is calculated after Rüpke et al. (2004).
4. Total H₂O recycling rate equals the sum of water recycling rates through sediments, basaltic crust and lithospheric mantle.

well-constrained. Uncertainties caused by this simplification might be insignificant due to the relative shallower depths of newborn fractures. We emphasize, however, any estimate of the lateral extent of serpentinization that accounts for an increase in fault density will fall between that estimated using a baseline fracture density (minimum bound) and that estimated by assuming that the lateral extent of serpentinization is 100% (maximum bound; previous paragraph).

To estimate the lateral extent of serpentinization associated with reactivation of normal faults in the bending zone, we consider two cases. In one case, the depth extent of every fault plane was assumed to reach a constant maximal value (equal to the serpentinization depth here) instantaneously when the fault initiates (30 km away from the trench in this case). In another, perhaps more realistic case, the depth extent of the fault is assumed to grow with time, beginning from zero thickness when the fault initiates and growing linearly with time as the fault approaches the trench. Results of our calculations are shown in Table 3. For serpentinization depth of ∼40 km (based on the minimum melting degree for FRO peridotites and an assumed paleo-potential temperature of 1350 °C), the resulting global recycling rate of water due to serpentinization of normal faults in bending zones is ∼1.2×10^{19} kg/Ma for the constant fault depth scenario and ∼8.0×10^{18} kg/Ma for the scenario in which the fault depth increases linearly with time.

We conclude with a few caveats. The validity of the estimated water recycling rates depends on the validity of derived paleo-melting depths of FRO peridotites which further depends on our choice of mantle potential temperature. It also depends on the validity of equating

the paleo-melting depths of FRO peridotites to their paleo-serpentinization depths. The validity of the global extrapolation also depends on whether the serpentinization depth of FRO peridotites can be used representatively for the global oceanic lithosphere. Water recycling rates for the subduction of serpentinized transform faults (Fig. 4A and Table 3, 1st conlum) could have been overestimated by taking the average age of subducting oceanic lithosphere (∼75 Ma) as diffusion timescale considering fractures developed near mid-ocean ridge could close up as the plate ages. Water recycling rates for both the subduction of serpentinized transform faults (Fig. 4A and Table 3, the 1st column) and subduction of serpentinized normal faults (Fig. 4C and Table 3, 2nd and 3rd column) could also have been overestimated by assuming that all serpentinized mantle peridotites contain 12 wt.% H₂O. Further uncertainties arise from the use of a constant H₂O diffusion coefficient (Macdonald and Fyfe, 1985) and the assumed fracture distribution patterns, which are not well-constrained. Despite all these potential uncertainties, we feel that our approach is justified insofar as we are seeking an order-of-magnitude constraint on the role of serpentinization in the whole Earth hydrologic cycle.

5.4.2. A steady-state ocean hypothesis

In this section, we try to place these estimates of water recycling through serpentinization into a more useful context by considering the water exchange between the ocean (the biggest water reservoir of the hydrosphere) and the Earth's deep interior. The total amount of mineralogically bound water associated with sediments and altered oceanic crust being recycled at

subduction zones is $\sim 1.9 \times 10^{17}$ (calculated from Plank and Langmuir (1998) and 5.4×10^{17} kg/Ma (calculated from Rüpke et al. (2004)), respectively (this estimate ignores pore waters, which are largely released in the accretionary prism). Water recycling rate estimated by Peacock (1990) are slightly different (0.7×10^{17} kg/Ma for sediments and 8.0×10^{17} kg/Ma for altered oceanic crust), but all of these recycling fluxes are an order of magnitude or more lower than our estimated contribution from serpentinized oceanic lithospheric mantle, underscoring the importance of the latter.

We can now compare these recycling fluxes of water at subduction zones to the volcanic dewatering fluxes into the Earth's hydrosphere and atmosphere. Volcanic dewatering rates were estimated from the global volcanic CO_2 degassing rate at different tectonic settings (Marty and Tolstikhin, 1998) and the average CO_2/H_2O ratio of volcanic gases emanated in these tectonic settings (Symonds et al., 1994). Details of our calculations are shown in Appendix B. Results of water recycling rates and volcanic dewatering rates are shown in Tables 3 and 4 separately. The volcanic dewatering rates correspond to 2.9×10^{18}, 2×10^{17}, and $<2.5 \times 10^{17}$ kg/Ma for convergent, divergent and hotspot settings, respectively. The total volcanic dewatering rate lies somewhere between 3.1 and 3.4×10^{18} kg/Ma. To check the validity of these estimates, a different method was used to calculate the dewatering rate at mid-ocean ridge (divergent tectonic setting). If we took the average extent of melting beneath mid-ocean ridges to be ~ 10 wt.% (Klein et al., 1991; Forsyth, 1993), the average thickness of basaltic crust (of density 2.7 g/cm^3) to be ~ 6 km, the global mid-ocean ridge length to be $\sim 67,338$ km (Bird, 2003), the average spreading rate to be ~ 46.6 km/Ma (Bird, 2003) and the average water content in N-MORB sources to be ~ 150 ppm (Michael, 1988; Michael, 1995; Danyushevsky et al., 2000; Saal et al., 2002), the calculated dewatering rate is $\sim 1.5 \times 10^{17}$ kg/Ma, consistent with the value (2×10^{17} kg/Ma) estimated from volcanic CO_2 degassing rate.

It can be seen that recycling of mineralogically bound water in oceanic sediments and oceanic crust is significantly lower than the global volcanic dewatering rate. If there were no other pathways for water to be returned into the Earth's interior, we would be forced to conclude that there is a net water loss from the Earth's interior, and the hydrosphere volume would be far from steady-state. This imbalance would also imply that the oceans have been growing in size through time. However, if we consider serpentinite subduction as an additional component of water recycling, we find that the total recycling rate of water through subduction (sediments, oceanic crust, and serpentinized lithospheric mantle) falls within 2.3 to 8.7×10^{18} kg/Ma (using a mantle potential temperature of 1350 °C). This is of the same order of magnitude as the global volcanic degassing rate (~ 3.1 to 3.4×10^{18} kg/Ma). Unfortunately, we are unable to determine what proportion of mineralogically bound water in subducting lithosphere is released to convergent margin volcanoes and what proportion remains behind and is subducted into deeper portions of the mantle. However, the simplest conclusion is that the rough match between the subduction input of water to the Earth's interior and the volcanic output of water from the interior suggests that the ocean volume of water may be and has been roughly at steady-state. In some sense, this conclusion may not be surprising given that extremely large fluctuations in sea-level have not been seen. However, our findings represent the first observation-based calculations that actually confirm the notion of a steady-state ocean. We note that had we used a mantle potential temperature of 1300 °C, the estimated serpentinization depth would decrease from 40 km to ~ 20 km (Fig. 7) and the estimated total water recycling rate would drop to 1.5 to 4.5×10^{18} kg/Ma (Table 3). This is still within the same order of magnitude as the global volcanic degassing rate (~ 3.1 to 3.4×10^{18} kg/Ma).

5.4.3. Implications for secular evolution of water

If our generalizations and interpretations of the data are valid, then the concept of a steady-state ocean has important consequences. An obvious question is whether the water lost at hotspots represents primordial water or recycled water from the Earth's hydrosphere? Again, the uncertainties in our calculations preclude us from quantitatively evaluating the origin of water in hotspot dewatering. However, the notion of a steady-state ocean suggests that it may be worth considering the possibility that the water budget of the Earth's interior is also at steady-state. If so, the water released at hotspots may simply be recycled water (Dixon et al., 2002).

If the water contents of the Earth's hydrosphere and interior are presently at steady-state, the next obvious question is when and how long did it take to attain steady-state in the hydrosphere and Earth's interior? The answer to this question may be of first-order importance to

Table 4
Global volcanic dewatering rate

Global volcanic dewatering rate	Value	Unit
Convergent-plate volcanoes	2.9×10^{18}	kg/Ma
Divergent-plate volcanoes	2.0×10^{17}	kg/Ma
Hot-spot volcanoes	$\leq 2.5 \times 10^{17}$	kg/Ma
Total	3.1 to 3.4×10^{18}	kg/Ma

understanding the thermal evolution of the Earth and possible secular evolution in the style of convection and plate tectonics. This is because water strongly influences the viscosity of the mantle (Hirth and Kohlstedt, 1996) and the extent of partial melting in the uppermost mantle (Asimow and Langmuir, 2003). For example, a completely dehydrated mantle could be 100 times more viscous than a water-saturated mantle at a given temperature (Hirth and Kohlstedt, 1996). This would result in an instantaneous Rayleigh number 100 times higher for a wet mantle if all other variables (such as internal mantle temperature) remain the same. The effect of water in depressing the solidus would result in greater degrees of melt extraction, which would be accompanied by greater losses of heat at the surface of the Earth due to the release of latent heat associated with melting and the advective transport of this melt and hence heat to the surface of the Earth. All other variables remaining the same, a wetter mantle would allow for more efficient heat loss (by promoting melting) at the upper thermal boundary layer of the convecting mantle. Our considerations, of course, only refer to the instantaneous effects of water. The overall effects on the Earth's thermal evolution, however, require an investigation of how water, rheology, melting, and convection are dynamically linked.

In this context, it will be important to incorporate the extent to which oceanic lithospheric mantle is serpentinized as this is the dominant mechanism of re-introducing water into the mantle. It will also be important to consider how the extent of serpentinization varies with time, or more specifically, varies with the thermal state of the Earth. Serpentinization is temperature-sensitive (Evans, 1977). Thus, in a hotter Earth, in which the age of subducting slabs is very young, extensive serpentinization of the oceanic lithospheric mantle might not occur because the temperature of subducting lithosphere may be too hot for formation of serpentine. Could the influence of serpentinization have increased since the Archean?

6. Conclusions

The petrology and geochemistry of serpentinized harzburgites from the Feather River Ophiolite in northern California were investigated. The serpentinized peridotites have major and trace-element signatures, which are dominantly consistent with an origin by hydrothermal addition of seawater into ultramafic protoliths within oceanic lithospheric mantle. There is little to no evidence for addition of higher temperature fluids associated with subduction-related metamorphic fluids or low temperature seawater alteration in a very high water/rock ratio environment, such as in the case of exhumed mantle at the seafloor. It is thus concluded that serpentinization of the Feather River ophiolite occurred during structural residence in intact oceanic lithosphere and hence prior to accretion or obduction onto the continent. Assuming that the FRO peridotites originally formed in a passive upwelling regime, paleo-depths of serpentinization were inferred to correspond to paleo-melt extraction depths of the ultramafic protoliths. The latter were estimated from major- and trace-element systematics and simple melting models. These constraints on the depth extent of serpentinization (∼40 km) were combined with simple models for estimating the lateral extent of serpentinization under the assumption that serpentinization is associated with faults and fractures. The global water recycling rate of serpentinized oceanic lithospheric mantle was estimated and shown to be roughly ten times larger than that associated with mineralogically bound water in subducting sediments and altered oceanic crust. The global water recycling rate, after accounting for serpentinization of the lithospheric mantle, is found to be of the same order-of-magnitude as the global dewatering rate associated with volcanism at convergent, divergent and intraplate environments.

Acknowledgments

Appendix A. Partial melting model

Melting and metasomatism

Rare-earth element concentrations in the peridotites were modeled by batch (Fig. 6B) or fractional melting (Fig. 6C). The former was modeled using the conventional batch melting equation. Fractional melting was simulated by incremental batch melting at 0.5 wt.% increments:

$$C_s = C_l D_{bulk}^F = \frac{C_s^{F-\delta} D_{bulk}^F}{(1-f) D_{bulk}^F + f} \tag{1}$$

where $f = \delta / (1 - (F - \delta))$, $D_{bulk}^F = \sum_{i=1}^{n} x_i(F) D_i$, δ (wt.%) is the increment of melting degree, f (wt.%) is the melting degree of the solid–liquid equilibration system, F (wt.%) is the cumulative melting degree of the bulk system (which includes incremental melts that have been

removed), C_s is the concentration in solid phase, C_l is the concentration in the melt, $C_s^{F-\delta}$ is the concentration in the solid residue of the previous step, n is the total number of mineral phases (olivine, clinopyroxene, orthopyroxene and spinel), $x_i(F)$ is the mineral mode as a function of melting degree F (Ghiorso et al., 2002), and D_i is the partition coefficient for a given mineral. Partition coefficients were taken from references in Niu and Hékinian (1997). To simulate mantle metasomatism (Fig. 6D), we considered the simple scenario in which a small amount of melt is added back to the residual peridotites. A 1% melt of a fertile lherzolite was taken as a plausible contaminant.

Appendix B. Water recycling rate and lateral extents of serpentinization

Serpentinization via transform faults in ocean basins
For the case in which the oceanic lithospheric mantle is serpentinized through oceanic transform faults (mechanism A in Fig. 4A, Table 3, the 1st column), an order of magnitude estimate of the global water recycling rate Q (kg/Ma) via subduction due to mantle serpentinization is

$$Q = \frac{2L_{diff}V \cdot (1\text{Ma}) \cdot Z_0 L_{tr} N \rho X_w}{1 - X_w} \qquad (2)$$

where $L_{diff} = (2Dt_{diff})^{1/2}$ is the approximate distance (km) to which seawater has diffused from the fracture into the wallrock, D (km^2/Ma) is the effective diffusivity of water in serpentinites (Macdonald and Fyfe, 1985), t_{diff} (Ma) is the time allowed for water diffusion (e.g., the time between fracture formation and subduction), V (km/Ma) is the average subducting velocity, Z_0 (km) is the estimated serpentinization depth (based on paleo-melting depths of FRO peridotites), L_{tr} (km) is the global trench length, N (fractures/km) is the number density of transform faults in ocean basins, ρ (kg/km^3) is the density of lithospheric mantle, and X_w (wt.%) refers to the water content in serpentinites (12 wt.%). In this particular case, t_{diff} is taken as the average age of subducting oceanic lithosphere (75 Ma).

Serpentinization via extensional normal faults re-activated in the bend of subducting slabs
For the case in which serpentinization of the oceanic lithospheric mantle occurs primarily by infiltration of seawater into extensional normal faults originally formed at the spreading centers but re-activated and exposed to seawater at the bend of a subducting slab (mechanism C in Fig. 4C), order of magnitude global water recycling rates were estimated for two end-member fault formation scenarios: 1) fracture depth increases linearly with time after its reactivation and is hence deepest just before the

slab meets the trench (Table 3, the 4th column), and 2) fracture depth is constant from the outset (Table 3, the 3rd column). We have assumed a baseline extensional fracture density N of 0.2/km (Ranero et al., 2003).

For the case of constant fracture depth Z_0 (Table 3, the 3rd column), the water recycling rate is

$$Q = 2Z_0 L_{diff} NV \cdot (1\text{Ma}) \cdot \rho \frac{X_w}{1 - X_w} \qquad (3)$$

where L_{diff} is the diffusion distance into the wallrock over the time elapsed t_{diff} between initiation of bending and eventual subduction and all other variables retain the same definitions as in Eq. (2). It is assumed that the bending zone is initiated 30 km from the trench (Ranero et al., 2003), hence $t_{diff} = 30$ km/V.

For the case in which fracture depth increases with time (Table 3, the 4th column), we assume a linear growth rate for simplicity. A rough estimate of Q is then given by

$$Q = 2L_{tr}NV \cdot (1\text{Ma}) \cdot \rho \frac{X_w}{1 - X_w} \int_0^{Z_0} L_{diff}(Z)\mathrm{d}Z \qquad (4)$$

where $L_{diff}(Z) = (2Dt_{diff}(Z))^{1/2}$ is the mean lateral diffusion distance at depth Z (km) for a given fracture. In this case, $t_{diff}(Z)$ is the allowed water diffusion time at depth Z (from the moment when the fracture depth reaches Z until the fracture is subducted). This quantity can be expressed as, $t_{diff} = t_o - Z(t_o/Z_o)$ where t_o is the total time elapsed between initiation of bending and subduction (30 km/V), Z_o is the maximum serpentinization depth determined from our case study of the Feather River Ophiolite, and $(t_o/Z_o)^{-1}$ is an approximate linear growth rate of the fault depth.

Extensive lithospheric mantle serpentinization
For the case of laterally extensive serpentinization (Table 3, the 2nd column), which assumes the whole column of lithospheric mantle above the estimated serpentinization depth Z_0 is serpentinized, Q was calculated as follows

$$Q = \frac{Z_0 L_{tr}V \cdot (1\text{Ma}) \cdot \rho X_w}{1 - X_w} \qquad (5)$$

where symbols are as previously defined.

Global volcanic dewatering rate
The global volcanic dewatering rate Q_V (kg/Ma) was calculated using

$$Q_V = \sum_{i=1}^{3} Q_{CO_2}^i r_{\frac{H_2O}{CO_2}}^i \qquad (6)$$

where $Q_{CO_2}^i$ (kg/Ma) represents the volcanic CO_2 output from different tectonic settings (convergent, divergent

and intraplate environments (Marty and Tolstikhin, 1998)) and $r^i_{H_2O/CO_2}$ is the weight ratio of H_2O to CO_2 in volcanic gases (Symonds et al., 1994). Relevant data are given in Appendix Table A1.

Table A1

Parameter	Value	Unit	Reference
Parameter	Value	Unit	Reference
Length of bending zone	30	km	Ranero et al. (2003)
Average subduction rate (V)	62.3	km/Ma	Bird (2003)
Number density of extensional faults at bending zone (N)	0.2	Fractures/ km	Calculated from Ranero et al. (2003)
Global trench length (L_{tr})	51310	km	Bird (2003)
Lithospheric mantle density (ρ)	3.3×10^{12}	kg/km^3	
Water content of serpentinites (X_w)	12%	wt.%	
Number density of transform faults on oceanic floor (N)	0.002	Fractures/ km	Macdonald (2001)
Average age of subducting oceanic slab	75	Ma	
H_2O content in a column of oceanic sediment of 350 m thick	6.0×10^{10}	kg/km^2	Compiled by Rüpke et al. (2004) with data from Plank and Langmuir (1998)
H_2O content in a column of oceanic crust of 7 km thick	1.7×10^{11}	kg/km^2	Rüpke et al. (2004)
Estimated CO_2 flux from convergent-plate volcanoes	2.5×10^{12}	Mol/a	Marty and Tolstikhin (1998)
Estimated CO_2 flux from divergent-plate volcanoes	2.2×10^{12}	Mol/a	Marty and Tolstikhin (1998)
Estimated CO_2 flux from hot-spot volcanoes	3×10^{12}	Mol/a	Marty and Tolstikhin (1998)
H_2O/CO_2 ratio for convengent-plate volcanoes	65	Molar ratio	Calculated from Symonds et al. (1994)
H_2O/CO_2 ratio for divengent-plate volcanoes	5.0	Molar ratio	Calculated from Symonds et al. (1994)
H_2O/CO_2 ratio for hot-spot volcanoes	4.6	Molar ratio	Calculated from Symonds et al. (1994)
H_2O diffusion coefficient (at 300 °C) D	3.16×10^{-1}	km^2/Ma	Macdonald and Fyfe (1985)

References

Asimow, P.D., Ghiorso, M.S., 1998. Algorithmic modifications extending MELTS to calculate subsolidus phase relations. Am. Mineral. 83, 1127–1132.

Asimow, P.D., Langmuir, C.H., 2003. The importance of water to oceanic mantle melting regimes. Nature 421, 815–820.

Asimow, P.D., Hirschmann, M.M., Stolper, E.M., 2001. Calculation of peridotite partial melting from thermodynamic models of minerals and melts, IV. Adiabatic decompression and the composition and mean properties of mid-ocean ridge basalts. J. Petrol. 42, 963–998.

Barnes, J.D., Sharp, Z.D., 2006. A chlorine isotope study of DSDP/ODP serpentinized ultramafic rocks: insights into the serpentinization process. Chem. Geol. 228, 246–265.

Bird, P., 2003. An updated digital model of plate boundaries. Geochem. Geophys. Geosyst. 4 (3), 1027, doi:10.1029/2001 GC000252.

Brenan, J.M., Shaw, H.F., Ryerson, F.J., 1995. Experimental evidence for the origin of lead enrichment in convergent-margin magmas. Nature 378, 54–56.

Canil, D., 2004. Mildly incompatible elements in peridotites and the origins of mantle lithosphere. Lithos 77, 375–393.

Danyushevsky, L.V., Eggins, S.M., Fallon, T.J., Christie, D.M., 2000. H_2O abundance in depleted to moderately enriched mid-ocean ridge magmas. Part I: incompatible behaviour, implications for mantle storage, and origin of regional variations. J. Petrol. 41, 1329–1364.

Day, H.W., Moores, E.M., Tuminas, A.C., 1985. Structure and tectonics of the northern Sierra Nevada. Geol. Soc. Amer. Bull. 96 (4), 436–450.

Dixon, J.E., Leist, L., Langmuir, C., Schilling, J.-G., 2002. Recycled dehydrated lithosphere observed in plume-influenced mid-ocean-ridge basalt. Nature 420, 385–389.

Edelman, S.H., et al., 1989. Structure across a Mesozoic ocean-continent suture zone in the northern Sierra Nevada, California. Spec. Pap. - Geol. Soc. Am. 224 (56).

Eggins, S.M., et al., 1997. A simple method for the precise determination of >40 trace elements in geological samples by ICP-MS using enriched isotope internal standardisation. Chem. Geol. 134, 311–326.

Ehrenberg, S.N., 1975. Feather River ultramafic body, northern Sierra Nevada, California. Geol. Soc. Amer. Bull. 86, 1235–1243.

Evans, B.W., 1977. Metamorphism of alpine peridotite and serpentinite. Annu. Rev. Earth Planet. Sci. 5, 397–447.

Evans, B.W., 2004. The serpentinite multisystem revisited: chrysotile is metastable. Int. Geol. Rev. 46, 479–506.

Forsyth, D.W., 1993. Crustal thickness and the average depth and degree of melting in fractional melting models of passive flow beneath mid-ocean ridges. J. Geophys. Res. 98, 16073–16079.

Gammons, C.H., Wood, S.A., Williams, A.E., 1996. The aqueous geochemistry of rare earth elements and yttrium: VI. Stability of neodymium chloride complexes from 25 to 300 degrees C. Geochim. Cosmochim. Acta 60, 4615–4630.

Ghiorso, M.S., Sack, R.O., 1995. Chemical mass transfer in magmatic processes. IV. A revised and internally consistent thermodynamic model for the interpolation and extrapolation of liquid–solid equilibria in magmatic systems at elevated temperatures and pressures. Contrib. Mineral. Petrol. 119, 197–212.

Ghiorso, M.S., Hirschmann, M.M., Reiners, P.W., Kress, V.C., 2002. The pMELTS: a revision of MELTS for improved calculation of phase relations and major element partitioning related to partial melting of the mantle to 3 GPa. Geochem. Geophys. Geosyst. 3, doi:10.1029/2001GC000217.

Gill, J.B., 1981. Orogenic Andesites and Plate Tectonics. Springer–Verlag, Berlin.

Green, H.W., Houston, H., 1995. The mechanics of deep earthquakes. Annu. Rev. Earth Planet. Sci. 169–213.

Hacker, B.R., Peacock, S.M., 1990. Comparison of the Central Metamorphic Belt and Trinity terrane of the Klamath Mountains with the Feather River terrane of the Sierra Nevada. Spec. Pap. - Geol. Soc. Am. 255, 75–92.

Hacker, B.R., Peacock, S.M., Aber, G.A., Holloway, D., 2003. Subduction factory 2. Are intermediate-depth earthquakes in subducting slabs linked to metamorphic dehydration reactions? J. Geophys. Res. 108, doi:10.1029/2001JB001129.

Herzberg, C., 2004. Geodynamic information in peridotite petrology. J. Petrol. 45, 2507–2530.

Hirth, G., Kohlstedt, D.L., 1996. Water in the oceanic upper mantle; implications for rheology, melt extraction and the evolution of the lithosphere. Earth Planet. Sci. Lett. 144 (1–2), 93–108.

Hirth, G., Kohlstedt, D.L., 2004. Rheology of the upper mantle and the mantle wedge: a view from the experimentalists. In: Eiler, J. (Ed.), Inside the Subduction Factory. Geophys. Monogr. Ser. Am. Geophys. Union, pp. 83–106.

Johnson, K.T.M., Dick, H.J.B., Shimizu, N., 1990. Melting in the oceanic upper mantle: an ion microprobe study of diopsides in abyssal peridotites. J. Geophys. Res. 95, 2661–2678.

Katz, R.F., Spiegelman, M., Langmuir, C.H., 2003. A new parameterization of hydrous mantle melting. Geochem. Geophys. Geosyst. 4, doi:10.1029/2002GC000433.

Keppler, H., 1996. Constraints from partitioning experiments on the composition of subduction-zone fluids. Nature 380, 237–240.

Kinzler, R.J., Grove, T.L., 1992. Primary magmas of mid-ocean ridge basalts: 2. Applications. J. Geophys. Res. 97, 6097–6926.

Kirby, S.H., 1995. Interslab earthquakes and phase changes in subducting lithosphere. U.S. Natl. Rep. Int. Union Geod. Geophys. 1991–1994. Rev. Geophys., vol. 33, pp. 287–297.

Kirby, S.H., Engdahl, E.R., Denlinger, R., 1996. Intermediate-depth intraslab earthquakes and arc volcanism as physical expressions of crustal and uppermost mantle metamorphism in subducting slabs. In: Bebout, G.E. (Ed.), Subduction: Top to Bottom. Geophys. Monogr. Ser. Am. Geophys. Union, Washington, D.C., pp. 195–214.

Klein, E.M., Plank, T., Langmuir, C.H., 1991. Constraints on models for mantle melting beneath ocean ridges. RIDGE Events, vol. 2, pp. 11–12.

Kogiso, T., Tatsumi, Y., Nakano, S., 1997. Trace element transport during dehydration processes in the subducted oceanic crust: 1. Experiments and implications for the origin of ocean island basalts. Earth Planet. Sci. Lett. 148, 193–205.

Kohlstedt, D.L., Evans, B., Mackwell, S.J., 1995. Strength of the lithosphere: constraints imposed by laboratory experiments. J. Geophys. Res. 100, 17587–17602.

Komor, S.C., Elthon, D., Casey, J.F., 1985. Serpentinization of cumulate ultramafic rocks from the North Arm Mountain massif of the Bay of Islands ophiolite. Geochim. Cosmochim. Acta 49, 2331–2338.

Leeman, W.P., 1996. Boron and other fluid-mobile elements in volcanic arc lavas: implications for subduction processes. In: Bebout, G.E., Scholl, D., Kirby, S., Platt, J.P. (Eds.), Subduction: Top to Bottom. AGU Monograph, pp. 269–276.

Macdonald, K.C., 2001. Seafloor spreading: mid-ocean ridge tectonics. In: Steele, J., Thorpe, K.T. (Eds.), Encyclopedia of Ocean Science. Academic Press, pp. 1798–1813.

Macdonald, A.H., Fyfe, W.S., 1985. Rate of serpentinization in seafloor environments. In: Sharman, G.F., Francheteau, J. (Eds.), Tectonophysics. Oceanic Lithosphere, pp. 123–135.

Marty, B., Tolstikhin, I.N., 1998. CO_2 fluxes from mid-ocean ridges, arcs and plumes. Chem. Geol. 145, 233–248.

Mayfield, J.D., Day, H.W., 2000. Ultramafic rocks in the Feather River Belt, northern Sierra Nevada, California. In: Brooks, E.R., Dida, L.Tabilio (Eds.), California Department of Conservation, Division of Mines and Geology, Report: 122. Field guide to the geology and tectonics of the northern Sierra Nevada, pp. 1–15.

McCulloch, M.T., Gamble, J.A., 1991. Geochemical and geodynamical constraints on subduction zone magmatism. Earth Planet. Sci. Lett. 102, 358–374.

McDonough, W.F., Sun, S.-S., 1995. The composition of the Earth. Chem. Geol. 120, 223–253.

McKenzie, D., Bickle, M.J., 1988. The volume and composition of melt generated by extension of the lithosphere. J. Petrol. 29, 625–679.

Michael, P.J., 1988. The concentration, behavior and storage of H_2O in the suboceanic upper mantle: implications for mantle metasomatism. Geochim. Cosmochim. Acta 52, 555–566.

Michael, P., 1995. Regionally distinctive sources of depleted MORB: evidence from trace elements and H_2O. Earth Planet. Sci. Lett. 131, 301–320.

Moores, E.M., 1970. Ultramafics and orogeny, with models of the US Cordillera and the Tethys. Nature 228, 837–842.

Niu, Y., 1997. Mantle melting and melt extraction processes beneath ocean ridges: evidence from abyssal peridotites. J. Petrol. 38, 1047–1074.

Niu, Y., Hékinian, R., 1997. Basaltic liquids and harzburgitic residues in the Garrett Transform: a case study at fast-spreading ridges. Earth Planet. Sci. Lett. 146, 243–258.

O'Hanley, D.S., 1996. Serpentine: Records of Tectonic and Petrological History. Oxford University Press, New York.

O'Hanley, D.S., Wicks, F.J., 1995. Conditions of formation of lizardite, chrysotile, and antigorite, Cassiar, British Columbia. Can. Mineral. 33, 753–774.

Peacock, S.M., 1990. Fluid processes in subduction zones. Science 248, 329–337.

Peacock, S.M., Wang, K., 1999. Seismic consequences of warm versus cool subduction metamorphism: examples from southwest and northeast Japan. Science 286, 937–939.

Pearce, J.A., 1983. Role of the sub-continental lithosphere in magma genesis at active continental margins. In: Hawkesworth, C.J., Norry, M.J. (Eds.), Continental Basalts and Mantle Xenoliths. Shiva, pp. 230–249.

Plank, T., Langmuir, C.H., 1998. The chemical composition of subducting sediment and its consequences for the crust and mantle. Chem. Geol. 145, 325–394.

Presnall, D.C., Gudfinnsson, G.H., Walter, M.J., 2002. Generation of mid-ocean ridge basalts at pressures from 1 to 7 Gpa. Geochim. Cosmochim. Acta 66, 2073–2090.

Raleigh, C.B., 1967. Tectonic implications of serpentinite weakening. Geophys. J. R. Astron. Soc. 14, 113–118.

Ranero, C.R., Phipps Morgan, J., McIntosh, K., Reichert, C., 2003. Bending-related faulting and mantle serpentinization at the Middle America trench. Nature 425, 367–373.

Rüpke, L.H., Morgan, J.P., Hort, M., Connolly, J.A.D., 2004. Serpentine and the subduction zone water cycle. Earth Planet. Sci. Lett. 223, 17–34.

Saal, A.E., Langmuir, C.H., Perfit, M.R., 2002. Vapour undersaturation in primitive mid-ocean-ridge basalt and the volatile content of Earth's upper mantle. Nature 419, 451–455.

Saleeby, J., 1978. Kings River Ophiolite, Southwest Sierra Nevada foothills, California. Geol. Soc. Amer. Bull. 89 (4), 617–636.

Saunders, A.D., Tarney, J., Weaver, S.D., 1980. Transverse geochemical variations across the Antarctic Peninsula: implications for the genesis of calc-alkaline magmas. Earth Planet. Sci. Lett. 46, 344–360.

Sharp, Z.D., Barnes, J.D., 2004. Water-soluble chlorides in massive seafloor serpentinites: a source of chloride in subduction zones. Earth Planet. Sci. Lett. 226, 243–254.

Snow, J.E., Dick, H.J.B., 1995. Pervasive magnesium loss by marine weathering of peridotite. Geochim. Cosmochim. Acta 59, 4219–4235.

Stalder, R., Foley, S.F., Brey, G.P., Horn, I., 1998. Mineral-aqueous fluid partitioning of trace elements at 900–1200 °C and 3.0–5.7 Gpa: new experimental data for garnet, clinopyroxene, and rutile, and implications for mantle metasomatism. Geochim. Cosmochim. Acta 62, 781–1801.

Stolper, E., Newman, S., 1994. The role of water in the petrogenesis of Mariana trough magmas. Earth Planet. Sci. Lett. 293–325, 293–325.

Straub, S.M., Layne, G.D., 2003. The systematics of chlorine, fluorine, and water in Izu arc front volcanic rocks: implications for volatile recycling in subduction zones. Geochim. Cosmochim. Acta 67, 4179–4203.

Symonds, R.B., Rose, W.I., Bluth, G.J.S., Gerlach, T.M., 1994. Volcanic-gas studies: methods, results, and applications. In: Carroll, M.R., Holloway, J.R. (Eds.), Volatiles in Magmas. Reviews of Mineralogy. Mineralogical Society of America, pp. 1–66.

Tatsumi, Y., 1986. Migration of fluid phases and genesis of basalt magmas in subduction zones. J. Geophys. Res. 94 (4), 4697–4707.

Weisenberg, C.W., 1979. Structural Development of the Red Hill Portion of the Feather River Ultrmafic Complex, Plumas County, California. Rice University, Houston, TX, United States (USA). 181 pp.

You, C.-F., Castillo, P.R., Gieskes, J.M., Chan, L.H., Spivak, A.J., 1996. Trace element behavior in hydrothermal experiments: implications for fluid processes at shallow depths in subduction zones. Earth Planet. Sci. Lett. 140, 41–52.